

Dislocation saturation in slip rate driven processes and initial microstructure effects for large plastic deformation of crystals

Jalal Smiri^{*†}, Oğuz Umut Salman^{*}, and Ioan R. Ionescu^{*‡§}

version : July 24, 2025

Abstract

Dislocation-density-based crystal plasticity (CP) models are introduced to account for the microstructural changes throughout the deformation process, enabling more quantitative predictions of the deformation process compared to slip-system resistance-based plasticity models. In this work, we present a stability analysis of slip-rate-driven processes for some established dislocation density-based models, including the Kocks and Mecking (KM) model and its variants. Our analysis can be generalized to any type of dislocation density model, providing a broader framework for understanding the stability of such systems. We point out the existence of saturation dislocation densities and the essential role of initial dislocation density in distinguishing between hardening and softening responses. Since the initial microstructure, modeled through the dislocation density, could be related to the size or the sample preparation process, implicit size-dependent effects can also be inferred. To further explore these phenomena, we conduct numerical simulations of pillar compression using an Eulerian crystal plasticity framework. Our results show that dislocation-density-based CP models effectively capture microstructural evolution in small-scale materials, offering critical insights for the design of miniaturized mechanical devices and advanced materials in nanotechnology.

Keywords: crystal plasticity, dislocation density, slip rate driven processes, large deformations, pillars compression, size-effect

^{*}LSPM (UPR 3407 of CNRS), Université Sorbonne Paris Nord, 93430, Villetaneuse, France

[†]now at FEMTO-ST, Université Marie et Louis Pasteur, 25000-Besançon, France

[‡]IMAR, Romanian Academy, 10587-Bucharest, Romania

[§]corresponding author, ioan.r.ionescu@gmail.com

1 Introduction

Crystalline solids undergo plastic deformation when macroscopic stresses exceed critical thresholds. This non-recoverable deformation is primarily mediated by the nucleation, motion, and interaction of dislocations - line defects in the crystal lattice structure [1, 2]. These dislocations evolve within a complex energy landscape shaped by both applied stresses and multi-scale interactions, including long-range elastic fields and short-range core effects. Controlling crystal plasticity mechanisms is essential across numerous applications, including metal strengthening processes, forming operations [3], fatigue resistance enhancement [4, 5, 6], nano-scale manufacturing, and micro-pillar optimization for miniaturized mechanical components [7, 8, 9, 10, 11, 12].

This complexity in crystal plasticity spans multiple length scales, creating a hierarchical structure of deformation mechanisms. At the atomistic level, individual dislocation cores and their interactions with grain boundaries govern local plastic events [13]. These microscopic processes aggregate into mesoscale phenomena, including dislocation patterns, cell structures, and grain-level deformation. Remarkably, despite this underlying complexity, macroscopic plasticity often manifests as a smooth, continuous stress-strain response. This observation has led to the widespread adoption of continuum approaches that model plastic flow as a continuous spatio-temporal deformation mechanism in conventional engineering applications, effectively homogenizing the rich microstructural landscape.

Continuum Crystal Plasticity (CP) incorporates lattice-based kinematics into the classical continuum framework for modeling crystal plasticity. Its original mathematical formulation was introduced by Hill [14] and Hill and Rice [15], with initial applications by Asaro and Rice [16, 17] and Pierce, Asaro, and Needleman [18]. Since then, many authors have further developed CP theory (see [19] for a comprehensive overview). The classical continuum crystal theory of plasticity assumes that crystalline materials undergo irreversible flow when applied stresses exceed certain thresholds. This theory models the stress-strain response with continuous curves, implying that the heterogeneities are averaged out. This approach has been successful in reproducing key plasticity phenomena such as yield, hardening, and plastic shakedown.

Obviously, CP theory does not resolve individual plastic defects. Instead, dislocations are represented by continuously evolving incremental shear strains (slips) γ^s . This coarse representation conceals both short-range and long-range dislocation interactions. However, the simplified kinematics allows access to larger time and length scales, enabling the modeling of complex 3D systems with intricate geometries. The method can be im-

plemented in a Finite-Element Method (FEM) setup or in spectral methods, facilitating the modeling of various physical phenomena, from grain boundary evolution to pattern formation under cyclic loading [19, 20, 21, 22].

While traditional CP models use phenomenological constitutive laws, more advanced formulations incorporate dislocation-related effects, such as kink and shear-band formation [23]. These advanced models employ physics-based constitutive laws that rely on internal variables with micro-structural significance. Among these internal variables, dislocation density stands out in the literature (see for instance [24, 25, 26, 27, 28]) as the most crucial in the context of plasticity as primary carriers of plastic deformation. By incorporating dislocation densities as state variables, CP models can address numerous complex scenarios: interactions between dislocations and grain boundaries [29], prismatic slip in α -titanium alloys [30], deformation of single FCC crystals under high strains [31], size-dependent plastic flow [32], and precipitate-induced cyclic softening [33], among others.

Building upon these dislocation density-based crystal plasticity frameworks, the objective of this study is to perform a stability analysis of slip rate driven processes for several established models: the Kocks and Mecking (KM) model, Kocks-Mecking-Teodosiu model, Kocks-Mecking-Estrin model, and Cui-Lin-Liu-Zhuang (CLLZ) model. Our analysis aims to identify the conditions leading to the attainment of "saturation" states of dislocation densities in active slip systems. Additionally, we seek to evaluate the (linear) stability of these states to determine whether they demonstrate attractor characteristics, which would provide insight into the long-term (large deformation) evolution of microstructure under continued loading.

The stability analysis of dislocation densities (DD) provides essential insights into dislocation evolution across different initial microstructures, helping to identify the conditions under which material softening or hardening occurs. This finding is consistent with the conclusions in [34], which suggest that the initial microstructure controls the response of nanopillars, influencing the occurrence of size-effects. Notably, the dislocation density may be influenced by specimen size or sample preparation processes (see [35, 36]), potentially introducing implicit size-dependent effects. Nevertheless, dislocation-density based CP models can effectively capture the microstructural evolution observed in small-scale materials without explicitly incorporating size-dependent terms in the constitutive equations. This finding holds promising implications for the design of miniaturized mechanical devices and innovative materials in the rapidly evolving field of nanotechnology.

Building on our analytical treatment, we conduct numerical simulations of pillar com-

pression with varying initial dislocation density (i.e. initial microstructure) using an Eulerian crystal plasticity approach that effectively captures very large deformations. Our motivation stems from the burgeoning field of nanotechnology, where the production of nano-scale structures has underscored the importance of understanding material behavior at submicron levels [37]. The compression test considered remains a pertinent example for illustrating insights derived from dislocation stability analysis, including the saturation of defect concentrations, and the impact of pre-existing microstructural features, while also linking these insights with experimental findings.

The rest of the paper is organized as follows. In Section 2, we present the dislocation-density-based flow rules. In Section 3, we study the stability conditions of these rules and how they can be related to the initial microstructure. Finally, in Section 4, we introduce the Eulerian 2D model of crystal plasticity and we perform compression simulations on micro-pillar and explain our findings in terms of the stability of dislocation-density-based flow rules. In Section 5, we present our conclusions.

2 Dislocation-density based crystal plasticity models

Dislocation-density-based crystal plasticity models provide a framework for describing the evolution of material strength by explicitly accounting for the interactions and dynamics of dislocations. These models relate the flow stress to the dislocation density and its evolution, capturing key mechanisms such as dislocation storage, annihilation, and dynamic recovery. Among the widely used models, the Kocks and Mecking (KM) model establishes a fundamental relation between strain hardening and dislocation density evolution. Extensions such as the Kocks-Mecking-Teodosiu and Kocks-Mecking-Estrin models introduce additional mechanisms to refine the prediction of strain hardening and recovery processes. More recently, a single arm source (SAS) controlled plastic flow model further advances this framework by incorporating enhanced descriptions of dislocation interactions [38]. These models play a crucial role in simulating the mechanical response of crystalline materials under various loading conditions.

In dislocation-density-based crystal plasticity models, the mechanical response of crystalline materials is governed by the interplay between elastic and plastic deformations. To accurately describe large plastic deformations, the deformation gradient is often multiplicatively decomposed into an elastic and a plastic part, enabling the formulation of constitutive laws within a geometrically consistent framework. The evolution of plastic flow is then characterized by flow rules that define the relationship between the plastic velocity

gradient and the material behavior. These flow rules can be either rate-independent (plastic) or rate-dependent (visco-plastic), capturing different strain-rate sensitivities. The dislocation density evolution is directly linked to these flow rules, as the accumulation and annihilation of dislocations dictate the material's strain hardening or softening response. By incorporating dislocation-density-based hardening and recovery mechanisms, models such as the Kocks-Mecking, Kocks-Mecking-Teodosiu, Kocks-Mecking-Estrin, and CLLZ frameworks provide a physics-based approach to predict the evolving mechanical properties of crystalline materials under various loading conditions.

In the following, we present this framework in detail, outlining the governing equations, flow rules, and dislocation-density-based hardening and softening mechanisms that define the material response.

2.1 Multiplicative decomposition of the deformation gradient

Consider a single crystal at time $t = 0$, free of any surface tractions and body forces. We choose this configuration, denoted as \mathcal{K}_0 , as the reference configuration of the crystal. Let $\mathcal{K} = \mathcal{K}(t)$ be the current configuration at time t . The incorporation of lattice features is achieved through a multiplicative decomposition of the total deformation gradient \mathbf{F} into elastic and plastic components:

$$\mathbf{F} = \mathbf{F}^e \mathbf{P}. \quad (2.1)$$

This decomposition implies a two-stage deformation process. First, \mathbf{P} transforms the initial reference state \mathcal{K}_0 into an intermediate state $\tilde{\mathcal{K}}$, which is characterized by plastic deformation only, with no change in volume. The tensor \mathbf{P} is referred to as the (visco)plastic deformation with respect to the reference configuration of a material neighborhood of the material point X at time t . Then, \mathbf{F}^e brings the body to the final configuration \mathcal{K} through elastic deformation and rigid lattice rotation. Specifically, \mathbf{F}^e can be expressed as

$$\mathbf{F}^e = \mathbf{R} \mathbf{U}^e, \quad (2.2)$$

where \mathbf{R} denotes the rotation of the crystal lattice with respect to its isoclinic orientation.

Following [39], \mathbf{P} is assumed to leave the underlying lattice structure undeformed and unrotated, ensuring the uniqueness of the decomposition in (2.1). The unique feature of CP theory is its construction of the plastic component \mathbf{P} by constraining dislocation kinematics. Plastic flow evolves along pre-selected slip directions via volume-preserving lattice invariant shears, leaving the crystal lattice undistorted and stress-free [39, 40, 41].

We label crystal slip systems by integers $s = 1, \dots, N$, with N denoting the number of slip systems. Each slip system s is specified by the unit vectors $(\mathbf{b}_s^0, \mathbf{m}_s^0)$, where \mathbf{b}_s^0 is in the slip direction and \mathbf{m}_s^0 is normal to the slip plane in the perfect undeformed lattice. Since the viscoplastic deformation does not produce distortion or rotation of the lattice, the mean lattice orientation is the same in the reference and intermediate configurations and is specified by $(\mathbf{b}_s^0, \mathbf{m}_s^0)$, $s = 1 \dots N$.

The (visco)plastic deformation is due to slip only, with the slip contribution to the (visco)plastic deformation given by ([42], [43])

$$\dot{\mathbf{P}}\mathbf{P}^{-1} = \sum_{s=1}^N \dot{\gamma}^s \mathbf{b}_s^0 \otimes \mathbf{m}_s^0, \quad (2.3)$$

where $\dot{\gamma}^s = \dot{\gamma}^s(t)$ is the viscoplastic shear rate on slip system s .

2.2 Plastic and visco-plastic flow rules

In order to complete the model, we need to provide the constitutive equation for the slip rate $\dot{\gamma}_s$ as a function of τ_s , the stress component acting on the slip plane of normal \mathbf{m}_s in the slip direction \mathbf{b}_s . In the current configuration, τ_s is expressed as

$$\tau^s = \boldsymbol{\sigma} : \mathbf{M}_s, \quad (2.4)$$

where $\boldsymbol{\sigma} = \boldsymbol{\sigma}(t)$ is the Cauchy stress tensor acting in the current configuration \mathcal{K} while \mathbf{M}_s is

$$\mathbf{M}_s = (\mathbf{b}_s \otimes \mathbf{m}_s)^{symm}. \quad (2.5)$$

and $\mathbf{b}_s = \mathbf{F}^e \mathbf{b}_s^0$ and $\mathbf{m}_s = (\mathbf{F}^e)^{-T} \mathbf{m}_s^0$ are the slipping and normal in the Eulerian configuration. Note that $\{\tau^s\}_{s=1, \dots, N}$ are not independent; they belong to a fifth dimensional space of \mathbb{R}^N corresponding to the dimension of the space of deviatoric stresses.

To determine the shear strain rates $\dot{\gamma}_\alpha$ relative to the local stress, a constitutive law is needed. Various proposals exist, ranging from phenomenological to more physically based approaches. One simple phenomenological approach assumes that $\dot{\gamma}_\alpha$ depends on the stress only through the resolved shear stress τ^s .

In rigid-plastic formulations, it is assumed that the onset of plastic flow of a slip system s is governed by Schmid law: the slip system s is active if and only if $|\tau^s| = \tau_c^s$, i.e.

$$\dot{\gamma}_s(|\tau^s| - \tau_c^s) = 0, \quad \dot{\gamma}_s \tau^s \geq 0, \quad |\tau^s| - \tau_c^s \leq 0, \quad (2.6)$$

where τ_c^s is the slip resistance (also called critical resolved shear stress or CRSS). For a given time t , the τ_c^s are material constants. Thus, the planes $|\tau^s| = \tau_c^s$ are the facets of the current yield surface of the single crystal in the stress space. The associated internal plastic dissipation functional is neither strongly convex or differentiable and the solution could not be unique. Additional assumptions are needed in order to restrict the number of solutions.

One way to overcome this difficulty of determining the active slip systems problem is to adopt a rate-dependent approach for the constitutive response of the single crystal. A widely used rate-dependent (viscoplastic) model is the Norton-type model, which relates the shear strain rate $\dot{\gamma}^s$ on a slip system s to the resolved shear stress τ^s through a power-law (see Asaro and Needleman [44])

$$\dot{\gamma}^s = \dot{\gamma}_0^s \left| \frac{\tau^s}{\tau_c^s} \right|^n \text{sign}(\tau^s), \quad (2.7)$$

where $\dot{\gamma}_0$ is a reference shear strain rate, while the exponent n has a fixed value.

Another regularization of the Schmid law can be done by using a Perzyna-like viscoplastic law of the form:

$$\dot{\gamma}^s = \frac{1}{\eta_s} [|\tau^s| - \tau_c^s]_+ \text{sign}(\tau^s), \quad (2.8)$$

where η_s is the viscosity, which may depend on the slip rate, and $[x]_+ = (x + |x|)/2$ denotes the positive part of any real number x . Note that the viscoplastic flow rule (2.8) is the visco-plastic extension of the rigid-plastic Schmid law using an overstress approach. The physical motivation for the dependence of the viscoplastic shear rate on the overstress $(\tau^s - \tau_c^s)$ was provided by Teodosiu and Sidoroff [43] based on an analysis of the microdynamics of crystals defects.

2.3 Dislocation density hardening/softening models

The yield limits τ_c^s of each slipping system s can be considered as constants, but they can vary in time if hardening/softening effects are taken into consideration. A widely used model uses dislocation densities on slip planes, denoted by ρ^s , as internal variables to link the microstructure to macroscopic deformation. To be more precisely, the critical resolved shear stress vector $\boldsymbol{\tau}_c = (\tau_c^1, \dots, \tau_c^N)$ depends on the dislocation densities vector $\boldsymbol{\rho} = (\rho^1, \dots, \rho^N)$ as follows:

$$\boldsymbol{\tau}_c = \boldsymbol{\mathcal{T}}_c(\boldsymbol{\rho}). \quad (2.9)$$

For example, in the context of the Taylor model [45], and as proposed by Teodosiu and Raphanel [46] (see also [47]), the shear yield strength is expressed as :

$$\mathcal{T}_c^s(\boldsymbol{\rho}) = \tau_0^s + \alpha\mu b \sqrt{\sum_{p=1}^N d^{sp}\rho^p}, \quad (2.10)$$

where τ_0^s is the friction stress, α is a dimensionless parameter describing the mean strength of obstacles encountered by the mobile dislocation lines, b is the modulus of the burgers vector parameter that relates the discrete plastic deformation of crystalline materials to dislocation motion, μ is the shear modulus and d^{sp} is a dimensionless interaction matrix expressing the average strength of the interactions and reactions between slip systems.

2.4 Dislocation density evolution models

These internal variables represent microstructural features, with dislocation density being the most crucial in the context of plasticity. Dislocations are the primary carriers of plastic deformation, making dislocation density a key microstructural state variable.

The evolution of the dislocation density can be developed from a phenomenological (statistical) model. The dislocation density rate $\dot{\rho}^s$, which is proportional to the plastic slip rate $|\dot{\gamma}^s|$, is the sum of the dislocation multiplication rate \mathcal{M}^s and of the dislocation annihilation rate $-\mathcal{A}^s$:

$$\dot{\rho}^s = \frac{1}{b} (\mathcal{M}^s(\boldsymbol{\rho}) - \mathcal{A}^s(\boldsymbol{\rho})) |\dot{\gamma}^s|. \quad (2.11)$$

For instance in the model of Kocks-Mecking-Teodosiu [46, 48] the multiplication and annihilation rates are given by

$$\mathcal{M}^s(\boldsymbol{\rho}) = \frac{\sqrt{\sum_{p=1}^N a^{sp}\rho^p}}{k}, \quad \mathcal{A}^s(\boldsymbol{\rho}) = 2y_c\rho^s, \quad (2.12)$$

where y_c is the mean distance controls the annihilation of dislocations and k is a proportionality factor, it represents the number of obstacle before a mobile dislocation get stopped and a^{sp} is a dimensionless interaction matrix. The values of interaction a^{sp} coefficients are listed in the Table 1, which were determined from dislocation dynamics simulations [1, 49].

In the case of generalized Kocks-Mecking-Estrin model [50], which is *size-dependent*, the expressions for dislocation multiplication \mathcal{M}^s and annihilation rates $\mathcal{A}^s(\boldsymbol{\rho})$ are provided as follows :

$$\mathcal{M}^s(\boldsymbol{\rho}) = \frac{\tilde{K}_0}{D} + \tilde{K}_1\sqrt{\rho^s}, \quad \mathcal{A}^s(\boldsymbol{\rho}) = bK_2\rho^s, \quad (2.13)$$

a_0^{self}	$a_{cop}^{coplanar}$	a_{orth}^{Hirth}	$a_{gli}^{glissile}$	a_{lom}^{lomer}	$a_{col}^{collinear}$
0.122	0.122	0.07	0.137	0.127	0.625

Table 1: Values of the six independent interaction coefficients a_{ij} for FCC crystals.

where \tilde{K}_0 is a production rate controlling factor (dimensionless), D the average grain size, \tilde{K}_1 governs the rate of dislocation storage by the interaction with immobile dislocations and K_2 is a controlling factor of recovery by the annihilation of dislocations.

In an alternative size-dependent model called the CLLZ model [38], the multiplication and annihilation rates are :

$$\mathcal{M}^s(\rho) = \frac{1}{2\bar{\lambda}} + k_f \sqrt{\rho^s}, \quad \mathcal{A}^s(\rho) = y\rho^s + \frac{2\cos^2(\beta/2)}{D},$$

where the model parameters are : $\bar{\lambda}$ is the length of the statistically average effective Single Arm Source, k_f is a dimensionless constant and set at 10^{-2} , y is the effective mutual annihilation distance and set to be equal to $6b$, β the slip-plane orientation angle is the angle between the primary slip plane and the top surface of the single-crystal micro-pillars and D is the diameter sample.

In the dislocation density-based constitutive model of Kameda and Zickry [51] it is assumed that the total dislocation-density ρ^s can be decomposed, into a mobile dislocation-density, ρ_m^s , and an immobile dislocation-density ρ_{im}^s as $\rho_{tot}^s = \rho_m^s + \rho_{im}^s$. For both of them we deal with two evolution equations

$$\frac{d\rho_m^s}{dt} = \left(\frac{g_{sour}}{b^2} \frac{\rho_{im}^s}{\rho_m^s} - \frac{g_{minter}}{b^2} \exp\left(-\frac{H}{kT}\right) - \frac{g_{immob}}{b} \sqrt{\rho_{im}^s} \right) |\dot{\gamma}^s|,$$

$$\frac{d\rho_{im}^s}{dt} = \left(\frac{g_{minter}}{b^2} \exp\left(-\frac{H}{kT}\right) + \frac{g_{immob}}{b} \sqrt{\rho_{im}^s} - g_{recov} \exp\left(-\frac{H}{kT}\right) \rho_{im}^s \right) |\dot{\gamma}^s|$$

where g_{sour} represents the coefficient associated with the rise in mobile dislocation density attributed to dislocation sources, g_{minter} denotes the coefficient linked to the trapping of mobile dislocations resulting from interactions with forest intersections, cross-slip mechanisms around obstacles, or dislocation interactions, g_{recov} signifies the coefficient related to the rearrangement and annihilation of immobile dislocations, g_{immob} denotes the immobilization of mobile dislocations, H is the activation enthalpy, and k is Boltzmann's constant. Since only the immobile dislocation densities are responsible of the

hardening/softening effect and their evolution is independent of the mobile ones we can conclude that immobile dislocation-density ρ_{im}^s plays the same role as ρ^s in the previous models. Moreover, the equation of immobile dislocation density evolution has the same structure as the generalized Kocks-Mecking-Estrin model. For that we have to take $\frac{\tilde{K}_0}{D_m} = \frac{g_{minter}}{b} \exp(-\frac{H}{kT})$, $\tilde{K}_1 = g_{immob}$ and $K_2 = g_{recov} \exp(-\frac{H}{kT})$.

Finally, the hardening or softening effects, described by (2.9) and (2.11), depend on the evolution of the dislocation density ρ^s on all systems s , that derives from the balance between accumulation and annihilation rates.

3 Dislocation density attractors in slip driven processes

We aim here to analyze the stability of several established dislocation density-based models, including the Kocks and Mecking (KM) model, the Kocks-Mecking-Teodosiu model, the Kocks-Mecking-Estrin model, and the CLLZ model. The objective is to identify the conditions under which saturation states emerge in active slip systems. Furthermore, we assess the linear stability of these states to determine whether they exhibit attractor-like behavior.

3.1 Stability analysis and attractors

In this section we will consider a slip driven process, which in our context means that the slip functions $t \rightarrow \gamma^s(t)$ are given for a significant time period $[0, T]$ for all $s = 1, \dots, N$. The N slip systems can be classified between N_a active slip systems and N_i inactive slip systems ($N = N_a + N_i$). To be more precisely let $A_c \cup A_i$ be a partition of $\{1, \dots, N\}$ and let us denote by $\boldsymbol{\rho}_a$ the vector containing all active slip systems $\rho^s, s \in A_c$, for which $|\dot{\gamma}^s| > 0$, and by $\boldsymbol{\rho}_i$ the vector with all inactive slip systems $\rho^s, s \in A_i$, for which $\dot{\gamma}^s = 0$. Following (2.11) the dislocation densities of inactive slip systems will rest constant, i.e. $\boldsymbol{\rho}_i(t) = \boldsymbol{\rho}_i(0) = \boldsymbol{\rho}_i^0$, while the active ones will satisfy the following Cauchy problem

$$\begin{cases} \dot{\rho}^s(t) = \frac{1}{b} (\mathcal{M}^s(\boldsymbol{\rho}_a(t), \boldsymbol{\rho}_i^0) - \mathcal{A}^s(\boldsymbol{\rho}_a(t), \boldsymbol{\rho}_i^0)) |\dot{\gamma}^s(t)|, \\ \rho^s(0) = \rho_0^s, \quad s \in A_c. \end{cases} \quad (3.1)$$

Let $\dot{\gamma}^{ref}$ be a reference slip rate and let denote by $\gamma = \dot{\gamma}^{ref} t$ the reference slip. For simplicity we consider only constant slip rates, i.e. $\dot{\gamma}^s(t) = \dot{\gamma}^{ref} g_s$. Since the model considered here are time independent the differential system (3.1) can be recasted in

terms of γ as

$$\begin{cases} \frac{d\rho^s}{d\gamma} = \frac{1}{b} (\mathcal{M}^s(\rho_a(\gamma), \rho_i^0) - \mathcal{A}^s(\rho_a(\gamma), \rho_i^0)) |g^s|, \\ \rho^s(0) = \rho_0^s, \quad s \in A_c. \end{cases} \quad (3.2)$$

To describe the attractors of the dislocation density (also referred to as the "saturation dislocation density"), we first need to compute the stationary (or invariant) dislocation densities, denoted by the vector $\tilde{\rho}_a$, as the solution of the following system:

$$\mathcal{M}^s(\tilde{\rho}_a, \rho_i^0) = \mathcal{A}^s(\tilde{\rho}_a, \rho_i^0), \quad s \in A_c. \quad (3.3)$$

We remark that if $\rho_a^0 = \tilde{\rho}_a$ then $\rho_a(t) = \tilde{\rho}_a$ for all $t \in [0, T]$. The attractors are linearly stable stationary dislocation densities. One can characterize the stability of $\tilde{\rho}_a$ through the eigenvalues $\lambda^q(\tilde{\rho}_a, \rho_i^0)$, $q = 1, \dots, N_a$ of the matrix

$$S_{sp} = \left(\frac{\partial \mathcal{M}^s}{\partial \rho^p}(\tilde{\rho}_a, \rho_i^0) - \frac{\partial \mathcal{A}^s}{\partial \rho^p}(\tilde{\rho}_a, \rho_i^0) \right) |g^s|, \quad s, p \in A_c.$$

If

$$Re(\lambda^q(\tilde{\rho}_a, \rho_i^0)) < 0 \quad \text{for all } q = 1, \dots, N_a \quad (3.4)$$

then $\tilde{\rho}_a$ is linearly stable and it is an attractor, called in the next *saturation dislocation density* and denoted by ρ_a^{sat} . That means that there exists a neighborhood \mathcal{N} of ρ_a^{sat} such that if $\rho_a^0 \in \mathcal{N}$ then $\rho_a(t) \rightarrow \rho_a^{sat}$ and $\tau_c(t) \rightarrow \tau_c^{sat} = \mathcal{T}_c(\rho_a^{sat}, \rho_i^0)$.

3.1.1 Self interaction dislocations

To continue, we first consider the case where the dislocation interactions are limited to self interaction, which means that the dislocation multiplication and annihilation rates for the slip system s depend only on ρ^s , i.e. $\mathcal{T}^s(\rho) = \mathcal{T}^s(\rho^s)$, $\mathcal{M}^s(\rho) = \mathcal{M}^s(\rho^s)$, $\mathcal{A}^s(\rho) = \mathcal{A}^s(\rho^s)$ for all systems s . For Kocks and Mecking's model (2.12) "self interaction" means $d^{sp} = a^{sp} = 0$ for $s \neq p$.

For self interaction dislocations is no longer necessary to distinguish between the active and inactive systems as in the previous section. To find the stationary dislocation densities $\tilde{\rho}^s$ the nonlinear system (3.3) reduces to a nonlinear equation

$$\mathcal{M}^s(\tilde{\rho}^s) = \mathcal{A}^s(\tilde{\rho}^s) \quad (3.5)$$

while the condition (3.4), which assure that a stationary density is an attractor (or a

saturation density), reads

$$\frac{d}{d\rho} \mathcal{M}^s(\tilde{\rho}^s) < \frac{d}{d\rho} \mathcal{A}^s(\tilde{\rho}^s). \quad (3.6)$$

In the next we analyze three specific models: (KM), (KME) and (CLLZ).

i) For *Kocks and Mecking's model* (2.12) we found from (3.5) two stationary density values for each slip system $\tilde{\rho}^s = 0$, and $\tilde{\rho}^s = a^{ss}/(2y_c k)^2 = a_0^{self}/(2y_c k)^2$, but according to (3.6) only the second one is stable that means that we deal with a single attractor or saturation dislocation density ρ_{sat}^s which corresponds to a saturation CRSS $\tau_{c,sat}^s$.

$$\rho_{sat}^s = \frac{a^{ss}}{(2y_c k)^2}, \quad \tau_{c,sat}^s = \tau_0^s + \frac{\alpha \mu b \sqrt{d^{ss} a^{ss}}}{2y_c k} \quad (3.7)$$

τ_0	α	μ	b	y_c	k
11 MPa	0.25	76 GPa	0.245 nm	$3.36 \times b$	38

Table 2: The parameters of DD hardening/softening model for a FCC single crystal.

As an example, we have computed in Fig. 1 (left) the evolution of the dislocation density $\gamma \rightarrow \rho^s(\gamma)$ (i.e., the solution of the Cauchy problem (3.2)) for a FCC single crystal. Physical values, summarized in Table 2, are taken from [36, 52]. We consider 8 choices of the initial dislocation densities $\rho_0^s \in [1 \times 10^{12}, 5 \times 10^{15}]$, and set $a^{s,p} = 0$ for $s \neq p$, leading to the saturation values $\rho_{sat}^s = 3.1169 \times 10^{13}$ and $\tau_{c,sat}^s = 20.0774$ MPa, as mentioned in equation (3.7). Since the saturation value of dislocation density and CRSS is uniform across the gliding systems the plot concerns only one slip system with different initial DD.

Given the similarity between interaction matrix $a^{s,p}$ and $d^{s,p}$, we have assumed that $a^{s,p} = d^{s,p}$. We remark that the dislocation densities and the critical resolved shear stress are converging to saturation values, as predicted by the theory, with a softening effect for $\rho_0^s > \rho_{sat}^s$ and a hardening one for $\rho_0^s < \rho_{sat}^s$. Moreover, this convergence is effective for large values of slips (more than 50%), which are expected in the shear bands for instance.

ii) For *generalized Kocks-Mecking-Estrin (KME) model* [53] the formula of the saturation dislocation density is

$$\rho_{sat}^s = \left(\frac{\tilde{K}_1 + \sqrt{\tilde{K}_1^2 + 4 b K_2 k_0}}{2 b K_2} \right)^2 \quad \text{with} \quad k_0 = \frac{\tilde{K}_0}{D} \quad (3.8)$$

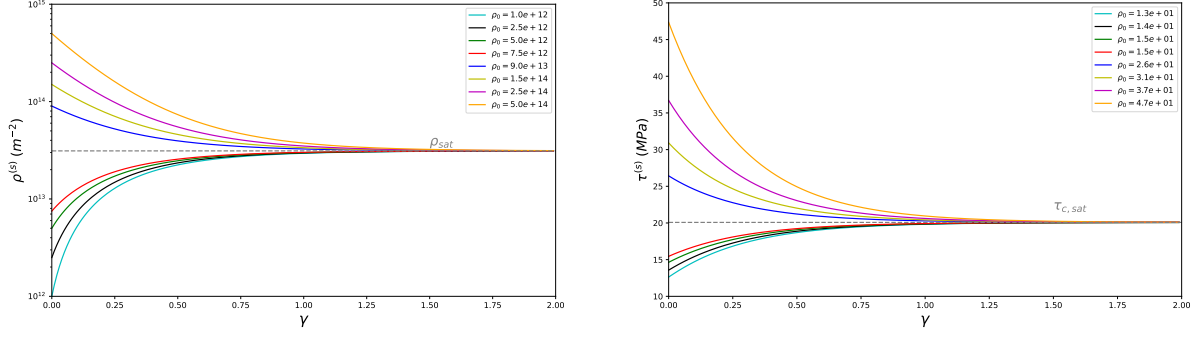


Figure 1: Evolution of a self-interacting system for eight different initial values ρ_0^s computed for the KM model. Left: dislocation density (in m^{-2}) over slip $\gamma \rightarrow \rho^s(\gamma)$. Right: shear yield strength (in MPa) over slip $\gamma \rightarrow \tau^s(\gamma)$.

iii) For them CLLZ model [38], the saturation dislocation density and corresponding critical resolved shear stress (CRSS) are given by:

$$\rho_{sat}^s = \left(\frac{k_f + \sqrt{k_f^2 + \frac{4by}{D} \left[\frac{1}{2\xi} - 2 \cos^2(\beta/2) \right]}}{2y} \right)^2, \quad (3.9)$$

$$\tau_{c,sat}^s = \tau_0^s + \alpha \mu b \sqrt{\rho_{sat}^s} + \frac{k \mu b}{\bar{\lambda}} \quad \text{with} \quad \xi = \frac{\bar{\lambda}}{D} \approx 0.3. \quad (3.10)$$

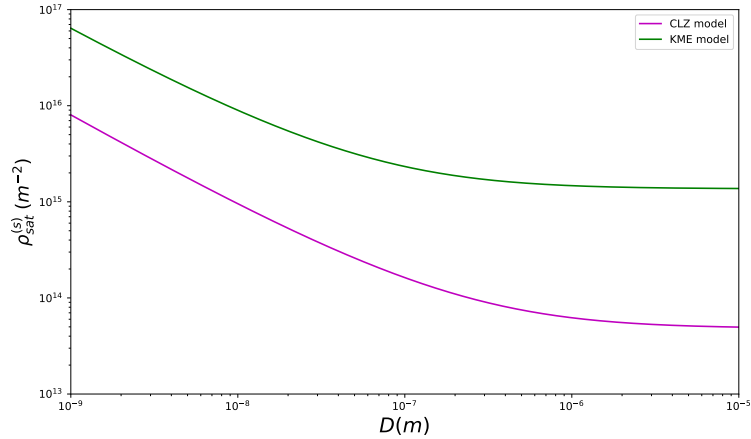


Figure 2: Saturation dislocation density ρ_{sat}^s (in m^{-2}) predicted by the KME model (3.8) and the CLLZ model (3.9) as a function of the scale parameter D (in m).

Figure 2 illustrates the influence of grain size D on the saturation dislocation density ρ_{sat}^s for the following settings: $b = 0.24$ nm, $\tilde{K}_1 = b \times 1.07 \times 10^{10}$, $k_2 = 289.63$, $\tilde{K}_0 = 3.8$ for (KME) model and $b = 0.24$ nm, $y = 6b$, $k_f = 0.01$, $\beta = 49^\circ$ for (CLZZ) model.

A pronounced size-effect is observed for both the KME and CLLZ models when the specimen diameter is below 10^{-7} m, where ρ_{sat}^s decreases rapidly as the diameter increases. Beyond this threshold, the size-effect becomes minor: the variation in ρ_{sat}^s slows down considerably, and both models tend toward a plateau near 5×10^{-6} m, where further increases in diameter have negligible impact. The angle β used in the CLLZ model corresponds to values measured in single-slip micro-pillar compression experiments. In the range $D \in [200 \text{ nm}, 10 \text{ }\mu\text{m}]$, relevant to such micro-pillar tests, the saturation dislocation density predicted by the three models (KM, KME, and CLLZ) remains largely insensitive to the grain size.

In conclusion for self interaction dislocations we can expect three different scenarios, depending of the initial condition ρ_0^s of the density dislocation: (i) If $\rho_0^s < \rho_{sat}^s$ then $\rho^s(t) \nearrow \rho_{sat}^s$ and we deal a with a hardening process $\tau_c^s(t) \nearrow \tau_{c,sat}^s$ up to a maximal critical resolved shear stress; (ii) if $\rho_0^s > \rho_{sat}^s$ then $\rho^s(t) \searrow \rho_{sat}^s$ and we deal a with a softening process $\tau_c^s(t) \searrow \tau_{c,sat}^s$ down to a minimal critical resolved shear stress; (iii) if $\rho_0^s \approx \rho_{sat}^s$ then $\rho^s(t) \approx \rho_{sat}^s$ and we deal a with a plateau $\tau_c^s(t) \approx \tau_{c,sat}^s$.

3.1.2 Cross-interacting dislocations

We now examine the Kocks and Mecking model as it applies to cross-interacting dislocations. This framework extends beyond self-interactions to account for the complex interplay between dislocations on different slip systems. The nonlinear system (3.3) for stationary dislocation densities $\tilde{\rho}_a$ reads:

$$\sum_{p \in A_c} a^{sp} \tilde{\rho}^p + \rho_{0,i}^s = (2y_c k)^2 (\tilde{\rho}^s)^2, \quad s \in A_c, \quad (3.11)$$

where

$$\rho_{0,i}^s = \sum_{p \in A_i} a^{sp} \rho_0^p, \quad s \in A_c.$$

Generally, the above system cannot be solved analytically and a numerical approach is needed. For instance one can use a Newton-Raphson method or to try to compute the local minimizers of the potential function

$$W(\rho_a) = \frac{(2y_c k)^2}{3} \sum_{p \in A_c} (\rho^p)^3 - \frac{1}{2} \sum_{s,p \in A_c} a^{sp} \rho^p \rho^s - \sum_{s \in A_c, p \in A_i} a^{sp} \rho_0^p \rho^s.$$

For the simplicity of the analysis we will suppose in the next that the slip rates $\dot{\gamma}^s = \dot{\gamma}^{ref}$ are the same in all active systems $s \in A_c$, i.e. $g^s = 1$. To see if a solution $\tilde{\rho}_a$ is an

attractor we have to compute the eigenvalues of $\tilde{\alpha}_s$ of the matrix

$$\tilde{A}_{sp} = \frac{a^{sp}}{\tilde{\rho}^s}.$$

Then the linear stability condition (3.4) reads

$$Re(\tilde{\alpha}_q) < 2(2y_ck)^2, \quad \text{for all } q = 1, \dots, N_a. \quad (3.12)$$

Let us mention here a sufficient condition which allow us to compute an analytic solution of (3.11). Let suppose that the sum of all cross-interaction coefficients corresponding to the active slip systems a^{sp} on a line s is the same for all lines, i.e.

$$\sum_{p \in A_c} a^{sp} = a_c, \quad \rho_{0,i}^s = \rho_{0,i}, \quad \text{for all } s \in A_c. \quad (3.13)$$

This assumption is satisfied for FCC crystals having their 12 slip systems active or specific active slip systems configurations. Supporting data examples are given in [54, 55].

If the above property is verified then there exists a uniform solution of (3.11), given by $\tilde{\rho}^s = \tilde{\rho}$ for all $s \in A_c$, where $\tilde{\rho}$ is $\tilde{\rho} = (a_c \pm \sqrt{a_c^2 + 4(2y_ck)^2 \rho_{0,i}}) / (2(2y_ck)^2)$. If $\rho_{0,i}$ is not vanishing then only one solution (corresponding to the sign $+$) is non-negative. If $\rho_{0,i} = 0$ (this is always the case if all slip systems are active $A_i = \emptyset$ or if the active and inactive systems are not interacting, i.e. $a^{sp} = 0$ for all $s \in A_c, p \in A_i$) then we deal with two uniform stationary dislocation densities: $\tilde{\rho} = 0$ and $\tilde{\rho} = a_c / (2y_ck)^2$.

To see if the stationary uniform density is an attractor we have to check the stability condition (3.12). We remark that if (3.13) holds then the largest eigenvalue of matrix \tilde{A}_{sp} , corresponding to the uniform eigenvector $(1, \dots, 1)$, is $\tilde{\alpha}^{max} = a_c / \tilde{\rho}$ and (3.12) holds always for $\tilde{\rho} > 0$. We deduce that for Kocks-Mecking model we deal with a uniform saturation dislocation density but (generally) a non-uniform saturation critical resolved shear stress, given by

$$\rho_{sat} = \frac{a_c + \sqrt{a_c^2 + 4(2y_ck)^2 \rho_{0,i}}}{2(2y_ck)^2}, \quad \tau_{c,sat}^s = \tau_0^s + \alpha \mu b \sqrt{\rho_{sat} \sum_{p \in A_c} d^{sp} + \sum_{p \in A_i} d^{sp} \rho_0^p}. \quad (3.14)$$

In order to see the role played by the level of inactive dislocation densities, denoted here by $\rho_{0,i}$, we have computed in Fig. 3 (left) the evolution of the dislocation density $\gamma^s \rightarrow \rho^s(\gamma^s)$ (i.e., the solution of the Cauchy problem (3.2)) for a single FCC crystal in the case of four active slip systems (denoted by $s = 1, 2, 3, 4$, i.e. $A_c = \{1, \dots, 4\}, A_i = \{5, \dots, 12\}$), considering two choices of inactive dislocation densities.

- $(\alpha) \rho_0^p = 10^{11} m^{-2}$ for all $p \in A_i$
- $(\beta) \rho_0^p = 10^{14} m^{-2}$, for all $p \in A_i$.

The interaction types between the four active slip systems are such that (1, 4) and (2, 3) are Lomer, (1, 3) and (2, 4) are orthogonal (Hirth), and (1, 2) and (3, 4) are coplanar. We remark that the assumption (3.13) is satisfied and the sum of all cross-interaction coefficients corresponding to the active slip systems is $a_c = a_{\text{cop}}^{\text{coplanar}} + a_{\text{orth}}^{\text{Hirth}} + a_{\text{lom}}^{\text{Lomer}}$, with $a^{sp} \approx d^{sp}$, values are given in Table 1. The other parameters ($y_c, k, \tau_0, \alpha, \mu$, and b) are listed in Table 2.

Thanks to the different initial dislocation density values, the initial values of τ_c^s are not identical across the active slip systems $s \in A_c$. Let us remark that, in our particular case, the four active slip systems evolve toward a uniform critical resolved shear stress (CRSS). This is due the fact that the sum of all cross-interaction coefficients a^{sp} along each active slip system s is identical for all four systems.

We have considered four uniform initial values of the four active dislocation densities $\rho_0^s = 1 \times 10^{13}, \rho_0^s = 8 \times 10^{13}, \rho_0^s = 1 \times 10^{14}$ and $\rho_0^s = 5 \times 10^{14} m^{-2}$ for all $s \in A_c$. We

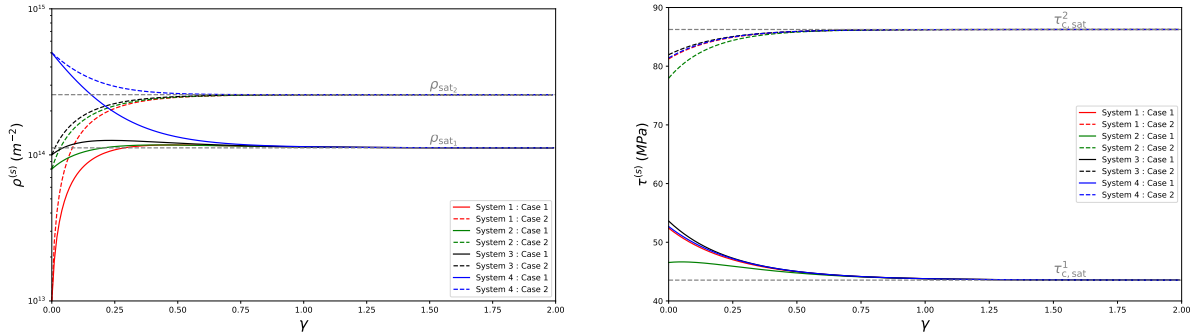


Figure 3: Evolution of a FCC single crystal cross interacting system (KM) model (3.14) for four different initial values ρ_0^s and two choices (α) and (β) of the level of inactive dislocation densities. Left: dislocation density (in m^{-2}) over slip $\gamma \rightarrow \rho^s(\gamma)$. Right: shear yield strength (in MPa) over slip $\gamma \rightarrow \tau_c^s(\gamma)$, for $s \in A_c$.

remark that the dislocation densities and the critical resolved shear stress are converging to saturation values $\rho_{\text{sat}} = 1.1307 \times 10^{14} m^{-2}$, $\tau_{\text{sat}} = 43.5395 \text{ MPa}$ for (α) and $\rho_{\text{sat}} = 2.584 \times 10^{14} m^{-2}$, $\tau_{\text{sat}} = 86.2565 \text{ MPa}$ for (β) , as is predicted by the theory. The value of the saturation is strongly dependent on the values of inactive dislocation densities. The level of inactive dislocation densities is essential in the evolution of yield limit. Indeed, as shown in Fig. 3 (right), in the first case we deal with a hardening process while in the second one we observe a softening behavior.

4 Saturation dislocation density in pillars compression

To see how the stability analysis presented earlier can provide insight into practical mono-crystal plasticity deformation processes, we conduct in this section numerical simulations of pillar compression. These simulations aim to demonstrate that the behavior of mono-crystal pillars under compression tests is strongly dependent on the initial dislocation density which could depend on the pillar size, particularly noticeable in FIB-prepared samples where the initial dislocation density decreases as the sample diameter increases [34].

4.1 The Eulerian crystal plasticity 2D model

The choice of the pillar compression processes to illustrate the above theory is due to the fact that the saturation dislocation density is effective only for large strains. We briefly describe here a simple 2D Eulerian crystal plasticity model (see [56]), that can capture very large deformations. It is acknowledged that the reduction from a 3D model to a 2D model, which incorporates only three slip systems, may result in the loss of some detailed information. Despite this simplification, the derived conclusions can still offer significant insights into the underlying physical phenomena.

4.1.1 Rigid-(visco)-plastic model

Since in applications involving large deformations and high strain rates, the elastic component of the deformation is small with respect to the inelastic one, it can be neglected and a rigid-viscoplastic approach can be adopted (see for instance, [57, 58, 59, 60, 61]). This means that we neglect the elastic lattice strain \mathbf{U}^e by supposing that $\mathbf{U}^e \approx \mathbf{I}$. This leads to the following decomposition of the deformation gradient \mathbf{F} (see [59]):

$$\mathbf{F} = \mathbf{R}\mathbf{P}. \quad (4.1)$$

Such a hypothesis is valid since during forming or other industrial processes, the elastic component of deformation is negligibly small (typically 10^{-3}) in comparison to the plastic component (typically $>10^{-1}$). It also to be noted that once the elastic/plastic transition is over the stress evolution in the grains is controlled by plastic relaxation, see [58]. Since elastic effects are neglected, we have $\mathbf{b}_s = \mathbf{R}\mathbf{b}_s^0$, $\mathbf{m}_s = \mathbf{R}\mathbf{m}_s^0$ and $\mathbf{b}_s \otimes \mathbf{m}_s = \mathbf{R}(\mathbf{b}_s^0 \otimes \mathbf{m}_s^0)\mathbf{R}^T$.

We seek to express the lattice evolution equations only in terms of vector and tensor fields associated with the current configuration. Let $\mathbf{v} = \mathbf{v}(t, x)$, the Eulerian velocity

field, \mathbf{L} the velocity gradient, \mathbf{D} the rate of deformation, and \mathbf{W} the spin tensor

$$\mathbf{L} = \mathbf{L}(\mathbf{v}) = \nabla \mathbf{v}, \quad \mathbf{D} = \mathbf{D}(\mathbf{v}) = (\nabla \mathbf{v})^{symm}, \quad \mathbf{W} = \mathbf{W}(\mathbf{v}) = (\nabla \mathbf{v})^{skew}. \quad (4.2)$$

If we denote by $\mathbf{M}_s = (\mathbf{b}_s \otimes \mathbf{m}_s)^{symm}$, $\mathbf{Q}_s = (\mathbf{b}_s \otimes \mathbf{m}_s)^{skew}$ then, using $\mathbf{L} = \dot{\mathbf{F}}\mathbf{F}^{-1} = \dot{\mathbf{R}}\mathbf{R}^T + \mathbf{R}\dot{\mathbf{P}}\mathbf{P}^{-1}\mathbf{R}^T$ and (2.3), the rate of deformation \mathbf{D} can be written as

$$\mathbf{D} = \sum_{s=1}^N \dot{\gamma}^s \mathbf{M}_s. \quad (4.3)$$

Taking the anti-symmetric part of \mathbf{L} , we obtain that the spin tensor is $\mathbf{W} = \dot{\mathbf{R}}\mathbf{R}^T + \sum_{s=1}^N \dot{\gamma}^s \mathbf{Q}_s$ and a differential equation for the rotation tensor \mathbf{R} :

$$\dot{\mathbf{R}} = (\mathbf{W} - \sum_{s=1}^N \dot{\gamma}^s \mathbf{Q}_s) \mathbf{R}. \quad (4.4)$$

The evolution equations (4.4) describe the evolution of the lattice in terms of vector and tensor fields associated with the current configuration.

4.1.2 In-plane deformation

The 3D system with a large number of slip systems N is too difficult to be analyzed from a theoretical or physical point of view. That is why, in many situations, a simplification could be useful for a better understanding of the complex phenomena which occur in crystal deformation. We will introduce here a two-dimensional model with $N = 3$ slip systems. In this case let us denote with ϕ and $-\phi$ the angles formed by slip system $r = 1$ with the other two systems $r = 2, 3$ and let θ be the angle formed by the slip system 1 with the Ox_1 axis (see Fig. 4). The three composite in-plane slip systems $\mathbf{b}_1, \mathbf{b}_2, \mathbf{b}_3$ are specified by the angles $\theta, \theta + \phi, \theta - \phi$. The main simplification for the 2-D problem

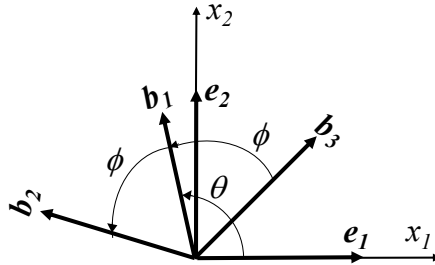


Figure 4: Two dimensional model with three slip systems.

comes from the lattice rotation \mathbf{R} which is now a rotation $\mathbf{R}(\theta, \mathbf{e}_3)$ with angle θ along

Ox_3 axis and we have $\mathbf{Q}_r = \frac{1}{2}((1, 0) \otimes (0, 1) - (0, 1) \otimes (1, 0))$ for all $r = 1, 2, 3$ and (4.4) has a much more simpler form

$$\dot{\theta} = \frac{\partial \theta}{\partial t} + \mathbf{v} \cdot \nabla \theta = \frac{1}{2} \left(\sum_{r=1}^3 \dot{\gamma}^r - \left(\frac{\partial v_1}{\partial x_2} - \frac{\partial v_2}{\partial x_1} \right) \right), \quad (4.5)$$

where $\mathbf{v} = (v_1, v_2)$ is the Eulerian velocity field. We have in mind two situations where this model is physically sound :

i) In-plane deformation of a FCC crystals : Rice [42] showed that certain pairs of the three-dimensional systems that are potentially active need to combine in order to achieve plane-strain deformation. For a F.C.C. crystal, with 12 potentially active slip systems, we consider Ox_3 axis to be parallel to $[110]$ in the crystal basis, which means that the plane-strain plane (Ox_1x_2) is the plane $[\bar{1}10] - [001]$. Some geometrical constraints (see [56]) must be satisfied such that $N = 3$ pairs of composite systems will give deformation in the plane (Ox_1x_2). The angle ϕ between the slipping system 1 and 2 is $\phi = \arctan(\sqrt{2}) \approx 54.7^\circ$. Since there are some scalar factors between the first two components of the in-plane systems and the 3-dimensional ones given by $q_1 = \frac{1}{\sqrt{3}}$, $q_2 = q_3 = \frac{\sqrt{3}}{2}$, the 2-D composite slipping rate $\dot{\gamma}^r$ corresponds to the 3-D slipping rate $\dot{\gamma}^k$ multiplied by $2q_r$. As it follows from [56] the 2-D yield limit τ_0^r corresponds to the 3-D yield limit τ_0^k divided by q_r while the 2-D viscosity η^r corresponds to the 3-D yield limit η^k divided by q_r^2 .

ii) Slip in the basal plane of a hexagonal crystal. Alternatively, this situation corresponds to hexagonal close-packed (HCP) crystals (such as Ti, Mg, Zr, etc) under plane strain, with the plane of deformation aligned with the basal plane (0001) of the hexagonal lattice. This situation has been considered experimentally in [62]. In this situation, the plastic strain is mainly accommodated by the three prismatic slip systems, i.e. the $(10\bar{1}0)\langle 1\bar{2}10 \rangle$ slip family. Each of those slip systems can act independently from the two others, as its strain is a plane strain. One might remark that combinations of other slip systems of HCP crystals from the basal and the pyramidal slip families could also lead to plane strain, but it would require significantly more energy, and therefore never occur. Thus, those slip families are not considered in this work. The prismatic slip systems are symmetric, leading to $\phi = \pi/3 = 60^\circ$.

4.2 Saturation dislocations of the 2D model

Let us analyze here more in details the simplified model to see how the methodology, previously described, is applied to examine the stability of dislocation density evolution

given by the KM model of a 2D model with three active slip systems.

For all numerical computations presented in this section we have used the 2D in-plane FCC model (i.e. $\phi = 54.7^\circ$) with the reference value τ_0 , along with all other material parameters used in the simulations, are provided in Tables 1 and 2. This yields to $\tau_0^1 = \tau_0/q_1 = 19.052$ MPa and $\tau_0^2 = \tau_0^3 = \tau_0/q_2 = 12.705$ MPa. A uniform initial dislocation density is chosen across all slip systems.

- (i) $\rho_0^s = \rho_0 = 9 \times 10^{13} \text{ m}^{-2}$ for all $s = 1, 2, 3$,
- (ii) $\rho_0^s = \rho_0 = 7.5 \times 10^{12} \text{ m}^{-2}$ for all $s = 1, 2, 3$.

4.2.1 Attractors of self interaction dislocations

In the context of self-interaction within the simplified model, the saturation of dislocation density and shear yield limit are determined using equation (3.7). Notably, the saturation dislocation density is uniform across the three slip systems and independent of specimen size, with the value $\rho_{sat}^s = 3.1169 \times 10^{13} \text{ m}^{-2}$, for all $s = 1, 2, 3$. Since the initial shear yield limit are different the saturation shear yield limit $\tau_{c,sat}^s$ is not uniform, exhibiting system-dependent values: $\tau_{c,sat}^1 = 28.13$ MPa, $\tau_{c,sat}^2 = \tau_{c,sat}^3 = 21.783$ MPa.

This distinction becomes evident in the two scenarios illustrated in Figure 5. In case (i), where the initial dislocation density of the 3 systems exceeds the saturation value, leading to softening: as $\rho^s \rightarrow \rho_{sat}^s$, the CRSS $\tau^s(t)$ declines toward its system-specific saturation value— $\tau_{c,sat}^1$ for system 1 and $\tau_{c,sat}^2$ for systems 2 and 3. (Although the model permits at most two simultaneously active slip systems, all three are shown as active in the figure for illustrative purposes.).

Conversely, in case (ii), representing a larger specimen, the system experiences hardening due to relatively low initial dislocation densities compared to the DD saturation ρ_{sat}^s . Both ρ^s and $\tau^s(t)$ increase: ρ^s tends toward the uniform saturation value ρ_{sat}^s , while $\tau^s(t)$ approaches its system-specific saturation value— $\tau_{c,sat}^1$ or $\tau_{c,sat}^2$ depending on the system in question.

4.2.2 Attractors of cross-interaction dislocations

In the analysis of cross-interactions, we utilize equation (3.11) to compute the stationary points. This is a nonlinear system which does not have, generally, analytical solutions. However in our simple model assumption (3.13) is valid and we can use (3.14). We have considered the dislocation interaction matrix associated with the three active slip systems

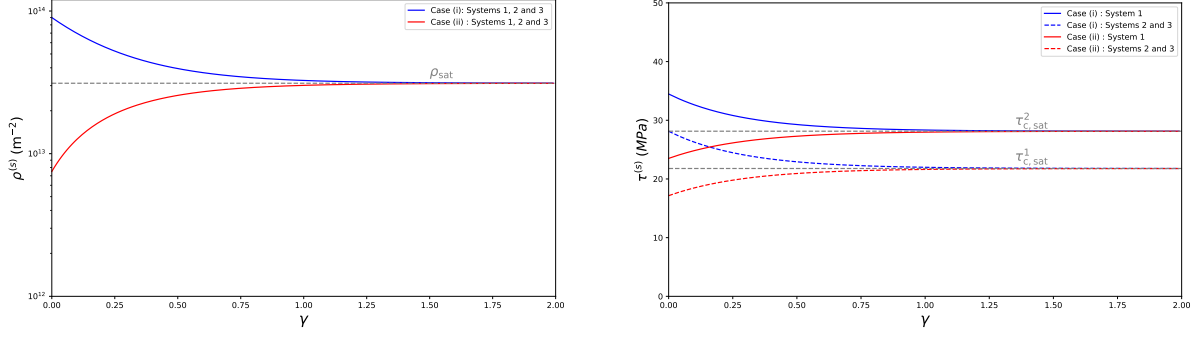


Figure 5: Evolution of the self-interaction 2-D model for two different choices of initial dislocation densities ρ_0^s , corresponding to case (i) (in blue) and case (ii) in (red). Left: dislocation density (from KM model in m^{-2}) over slip $\gamma \rightarrow \rho^s(\gamma)$. Right: shear yield strength (in MPa) over slip $\gamma \rightarrow \tau_c^s(\gamma)$ with $s = 1$ in solid line and $s = 2, 3$ in dashed line.

as follows: $a_{11} = a_{22} = a_{33} = a_0^{\text{self}}$ and $a_{12} = a_{13} = \beta = a_{\text{cop}}^{\text{coplanar}}$ and $a_{23} = \zeta = a_{\text{cop}}^{\text{coplanar}}$. Concerning the choice of active and inactive systems two cases, inspired from the FE computations of micro-pillars compression, will be considered in the next:

- (a) $A_c = \{1\}, A_i = \{2, 3\}$
- (b) $A_c = \{1, 2\}, A_i = \{3\}$

Case (a) has only one active system $s = 1$, hence $a_c = a_0$ and $\rho_{0,i} = \rho_0(\beta + \zeta)$ and we can compute the saturation values from (3.14) as:

$$\rho_{\text{sat}}^1 = \frac{a_0 + \sqrt{a_0^2 + 4(2y_c k)^2 \rho_0(\beta + \zeta)}}{2(2y_c k)^2}, \quad \tau_{c, \text{sat}}^s = \tau_0^s + \alpha \mu b \sqrt{\rho_{\text{sat}}^1 d^{s1} + (d^{s2} + d^{s3}) \rho_0}. \quad (4.6)$$

Figure 6 illustrates the response of the cross-interaction model (equation 4.6), showing the evolution of both dislocation density and shear yield strength with increasing slip, for two different initial dislocation densities. This allows for a direct comparison between case (i) in blue and case (ii) in red. The dislocation density evolution is shown only for the active slip system $s = 1$. For the inactive systems $s = 2$ and $s = 3$, dislocation densities remain constant throughout the deformation, resulting in flat lines that are not plotted here for clarity. Despite the inactivity of these systems, the corresponding critical resolved shear stresses (CRSS) still evolve due to cross-interaction effects; hence, CRSS curves are shown for all three systems. For system $s = 1$, we observe that the dislocation density evolves toward a saturation value that depends on the initial configuration. This is a key distinction from the self-interaction case, where the saturation dislocation density ρ_{sat}^s are independent of the initial state. The cross-interaction model thus captures a more

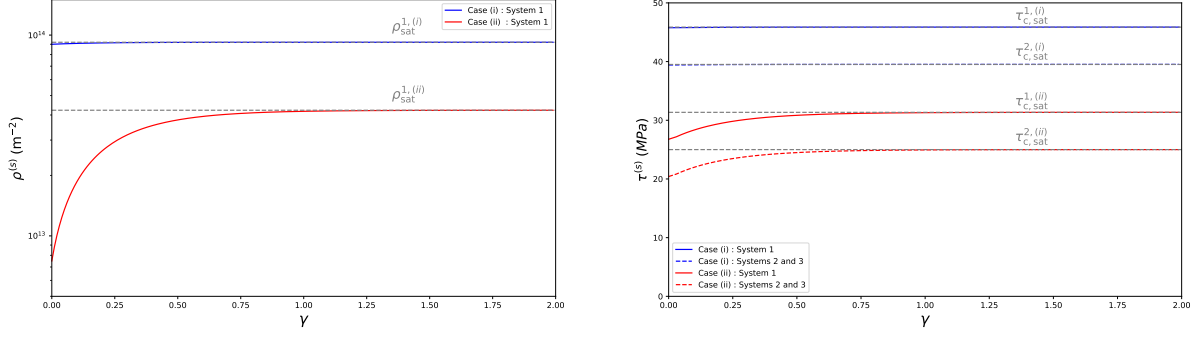


Figure 6: Evolution of the cross-interaction simplified model (4.6) in case (a) for two different initial choices of initial dislocation densities ρ_0 , corresponding to case (i) (in blue) and case (ii) (in red). Left: dislocation density (in m^{-2}) over slip $\gamma \rightarrow \rho^1(\gamma)$. Right: shear yield strength (in MPa) over slip $\gamma \rightarrow \tau_c^s(\gamma)$, shown for slip system $s = 1$ (solid line), and for $s = 2$ and $s = 3$ (dashed line; both curves are superimposed).

sensitive dependence of the hardening behavior on the initial micro-structural conditions. The dislocation density saturates at $\rho_{sat}^{1,(i)} = 9.26 \times 10^{13} \text{ m}^{-2}$ for case (i) and $\rho_{sat}^{1,(ii)} = 6.58 \times 10^{13} \text{ m}^{-2}$ for case (ii). In contrast, the dislocation densities in systems $s = 2$ and $s = 3$ remain constant during loading, and these constant values do not result from a saturation process.

It is also worth noting that several distinct saturation values are observed for the CRSS: two for system $s = 1$, corresponding to each initial configuration: $\tau_{c,sat}^{1,(i)} = 45.87 \text{ MPa}$ for case (i) and $\tau_{c,sat}^{1,(ii)} = 31.35 \text{ MPa}$ for case (ii), two for the inactive systems $s = 2$ and $s = 3$, which also correspond to the two cases $\tau_{c,sat}^{2,(i)} = \tau_{c,sat}^{3,(i)} = 39.51 \text{ MPa}$ for case (i) and $\tau_{c,sat}^{2,(ii)} = \tau_{c,sat}^{3,(ii)} = 25.00 \text{ MPa}$ for case (ii). The CRSS evolution in these inactive systems is instead driven solely by cross-interactions with the evolving dislocation density of system 1. This quasi-stationary dislocation structure across the three systems, maintained as slip increases, leads to a plateau-like mechanical response. This contrasts with the behavior observed in the self-interaction model, where softening is more pronounced due to the absence of cross-interaction effects.

Case (b) has two active system $s = 1, 2$, hence $a_c = a_0 + \beta$ and $\rho_{0,i} = \rho_0 \zeta$ and we can compute the saturation values from (3.14) as:

$$\rho_{sat}^1 = \rho_{sat}^2 = \frac{a_0 + \beta + \sqrt{(a_0 + \beta)^2 + 4(2y_c k)^2 \rho_0 \zeta}}{2(2y_c k)^2},$$

$$\tau_{c,sat}^s = \tau_0^s + \alpha \mu b \sqrt{\rho_{sat}^1 (d^{s1} + d^{s2}) + d^{s3} \rho_0}.$$

4.3 Numerical simulations setup

The compression test methodology is shown schematically in Figure 7. The aspect ratio between the micro-pillar initial high H_0 and its diameter D was chosen to be 2.5. The setting mimics the compression experiment commonly conducted on nano and micro scale samples. The (top) surface of the sample is in unilateral frictional contact (friction coefficient $\mu_f = 0.2$) with a rigid plate which moves with a small constant velocity $-V$ on y -axis, the plate movement continues until the sample's final height is reduced by 25% from the initial height, i.e. the engineering strain $\varepsilon^{engn} = (H_0 - H)/H_0$ is increasing up to $\varepsilon_{final}^{engn} = 0.25$. The other parts of the pillar which is not in contact with the upper plate are traction free whereas on the bottom the sample is fixed.

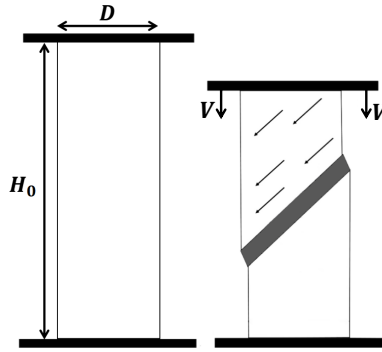


Figure 7: A schematic representation of micro-pillar compression and the formation of a shear band (in grey).

In all the simulations, the global rate of deformation is kept low at 0.5 s^{-1} , allowing the loading to be considered quasi-static. For the material coefficients of Nickel, all parameter values—except for the mass density $\rho^{\text{mass}} = 8900 \text{ kg/m}^3$ —are provided in Tables 2 and 1. These include the shear modulus, Burgers vector, the KM dislocation density evolution model parameters, as well as the slip system interaction matrix.

Initial dislocation densities. We used two different initial dislocation densities, denoted as (i) and (ii), and described in Section 4.2.

Initial orientation of the mono-crystal was chosen to be $\theta^0 = 65^\circ$.

Viscosity. The viscosity was chosen to be as small as possible (less than 1% of $\tau_0 H/V$) to ensure the convergence of the numerical scheme while maintaining the rate-independence of the mechanical model.

Time step. Since we are using an implicit numerical scheme, the chosen time step is relatively large and corresponds to a deformation of 0.1% between two time steps. As

a result, the computational cost is low, allowing the simulations to be performed on a personal computer.

Mesh. To capture the shear bands, we used an adaptive mesh technique based on the strain rate norm $\dot{\epsilon}_p = |\mathbf{D}|$, where ϵ_p is the cumulative plastic strain. This means that regions with a higher slip rate have a finer mesh, while regions outside have a coarser mesh. The ratio between the fine and coarse mesh sizes was 1/8. Figure 8, shows the distribution of cumulative plastic strain ϵ_p at $\varepsilon^{engn} = 15\%$ for three mesh refinement ratios. We found that for the ratio 1/8 is small enough to assure that the numerical results are not mesh-dependent.

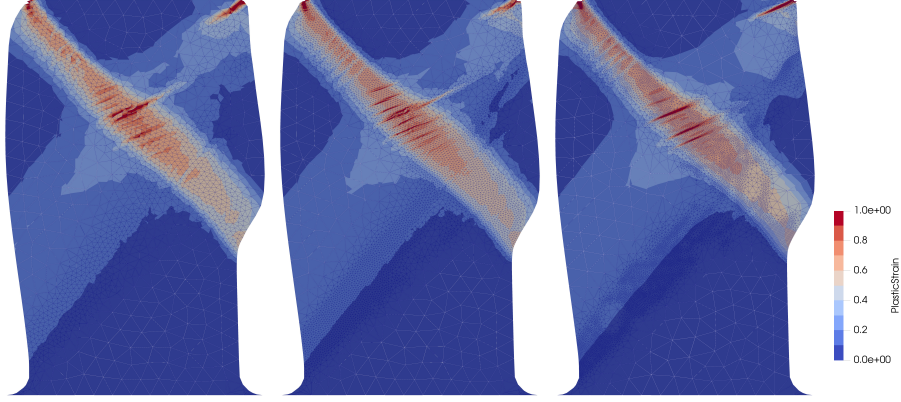


Figure 8: The computed distribution of cumulative plastic strain ϵ_p at $\varepsilon^{engn} = 15\%$ in case (i) for three different meshes with different ratio between the sizes of the fine and coarse meshes: 1/4 (left); 1/8 (middle); 1/16(right).

4.4 Numerical scheme used for the simulations

The main goal of this section is to recall the Eulerian numerical strategy proposed in [63] (see also [64]) for the rigid-visco-plastic crystal model used in this work. Time implicit (backward) Euler scheme is used for the field equations, which gives a set of nonlinear equations for the velocities \mathbf{v} and lattice orientation θ . At each iteration in time, an iterative algorithm is used in order to solve these nonlinear equations. Specifically, the variational formulation for the velocity field is discretized using the finite element method, while a Galerkin discontinuous method with an upwind choice of the flux is adopted for solving the hyperbolic equation that describes the evolution of the lattice orientation. One of the advantages of the proposed numerical strategy is that it does not require the consideration of elastic deformation since it is not based on an elastic predictor/plastic corrector scheme (e.g. [65]).

It is to be noted that in the case of the proposed rigid-viscoplastic model (2.8), numerical difficulties arise from the non-differentiability of the viscoplastic terms. That means that one cannot use finite element techniques developed for Navier-Stokes fluids. To overcome these difficulties the iterative decomposition-coordination formulation coupled with the augmented Lagrangian method of [66] was modified. The reason for this modification is that in the used crystal model, there is not co-axiality between the stress deviator and the rate of deformation as it is the case in the von-Mises (Bingham) model used in [66]. This type of algorithm permits also to solve alternatively, at each iteration, the equations for the velocity field and for the unit vectors that define the lattice orientation.

For vanishing viscosity, the adopted visco-plastic model contains as a limit case the inviscid Schmid law. Even that Schmid model is very stiff, for small viscosities (as for metals) and moderate strain rates the iterative decomposition coordination formulation coupled with the augmented Lagrangian method works very well and no instabilities are presents.

To include frictional effects in the algorithm, we first regularize the friction acting on the upper part of the micro-pillar. This was done (as in [67, 68]) by introducing a small frictional viscosity η_f in the Coulomb friction law as

$$[\mathbf{v}_T] = -\frac{1}{\eta_f} \left[1 - \frac{\mu_f [-\sigma_n]_+}{|\boldsymbol{\sigma}_T|} \right]_+ \boldsymbol{\sigma}_T, \quad (4.7)$$

where $[\mathbf{v}_T]$ is the relative tangential velocity, $\sigma_n, \boldsymbol{\sigma}_T$ are the normal and tangential stresses, μ_f is the frictional coefficient and $[x]_+ = (x + |x|)/2$. Note that using this regularization, the friction law has the same mathematical structure as the viscoplastic constitutive equation and we can use the same iterative decomposition-coordination formulation.

If the Eulerian domain \mathcal{D} has time variations then the above algorithm has been adapted to an ALE (Arbitrary Eulerian-Lagrangian) description of the crystal evolution. In this case is more convenient to have the same finite element Galerkin discontinuous meshes. This avoid the interpolation of the lattice orientation on the deformed mesh. As a matter of fact, the numerical algorithm proposed here deals only with a Stokes-type problem at each time step and the implementation of the Navier-Stokes equations in an ALE formulation is rather standard (see for instance [69, 70]).

4.5 Self interaction simulations

Firstly, we investigate the compression of pillars under the assumption of self-interaction to analyze the disparities in the mechanical response between the two cases defined in

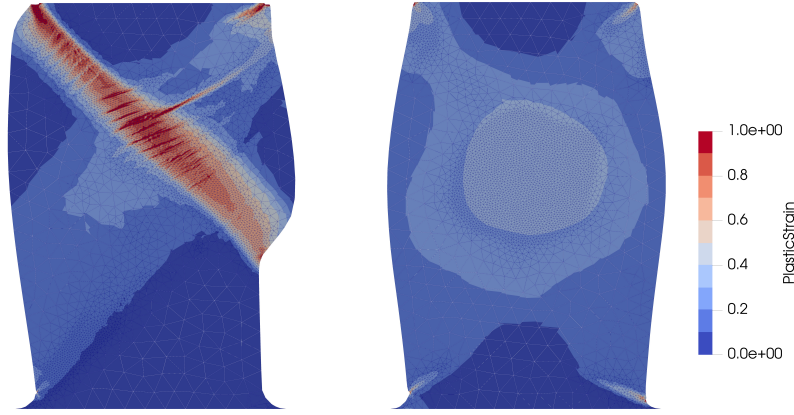


Figure 9: Pillar final deformation for the self interaction model. Accumulated plastic strain corresponding to $\epsilon^{engn} = 18\%$ for two choices of initial dislocation densities: case (i) (left) and case (ii) (right).

subsection 4.2 with two choices of the initial distribution of the dislocation densities corresponding to small and large specimen.

Final shape. As shown in Fig. 9, the micro-pillars exhibit qualitatively different deformation processes. In case (i), plastic deformation is localized, taking the form of a thin shear band that accumulates almost all the deformation (the accumulated plastic strain exceeds 100%), effectively separating two rigid regions. Conversely, in case (ii), the response is typical of conventional bulk materials, where the deformation is more homogeneous, leading to a barrel-shaped pillar.

Slip rates. Fig. 10 shows the spatial distribution in the micro-pillar of the slip rates corresponding to the 3 slip systems at different levels of engineering deformation. Slip system 1 remains active throughout the entire deformation process, irrespective the case considered. The activity of system 1 concentrates in the middle of case (ii) (larger specimen), while in case (i), it localizes within the shear band. On the other hand, system 2 is active only for case (ii) and at higher engineering deformation levels (beyond 10%). In the case (i) the activity of system 2 is somewhat limited and confined to a narrow bands. Notably, system 3 remained inactive across all cases.

Evolution of dislocation densities. We show the dislocation density evolution, in Fig. 11. For slip systems 2 and 3, which have small slip rates, we observe no significant variation. The dislocation density associated with slip system 1 decreases as deformation progresses in case (i) (small sample), while it increases in case (ii) (larger sample), as expected from the stability analysis described in subsection 4.2. As it follows from Figure 5 right, in case (i) (smaller pillar), we expect a softening deformation process, whereas in case (ii) (larger pillar), a hardening deformation process occurs.

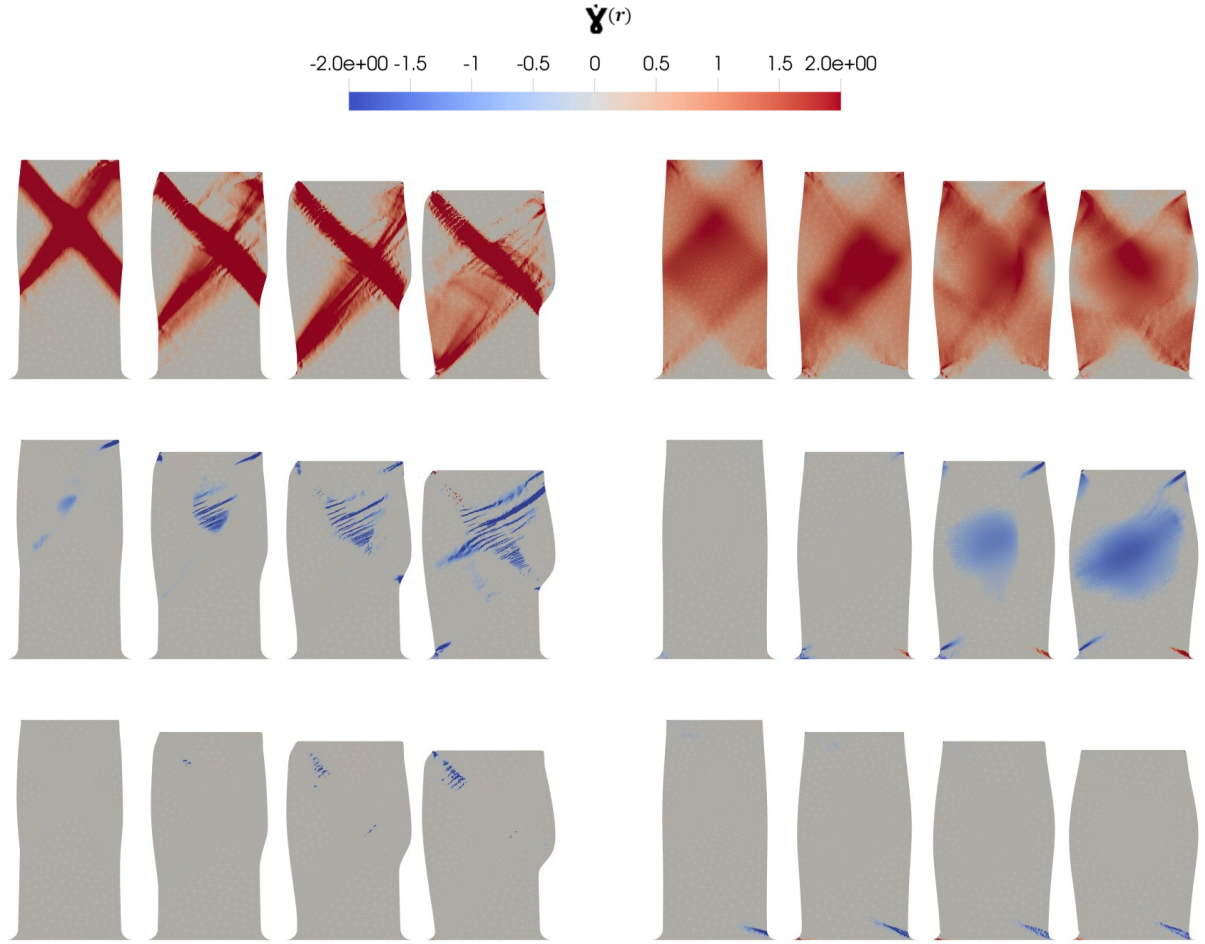


Figure 10: Pillar deformation for the self interaction model. The slip rates $\dot{\gamma}_1$ (up), $\dot{\gamma}_2$ (middle) and $\dot{\gamma}_3$ (bottom) distribution (in sec^{-1}) at different levels of engineering deformations (5%, 10%, 14% and 18%) for two choices of initial dislocation densities: case (i) (left) and case (ii) (right).

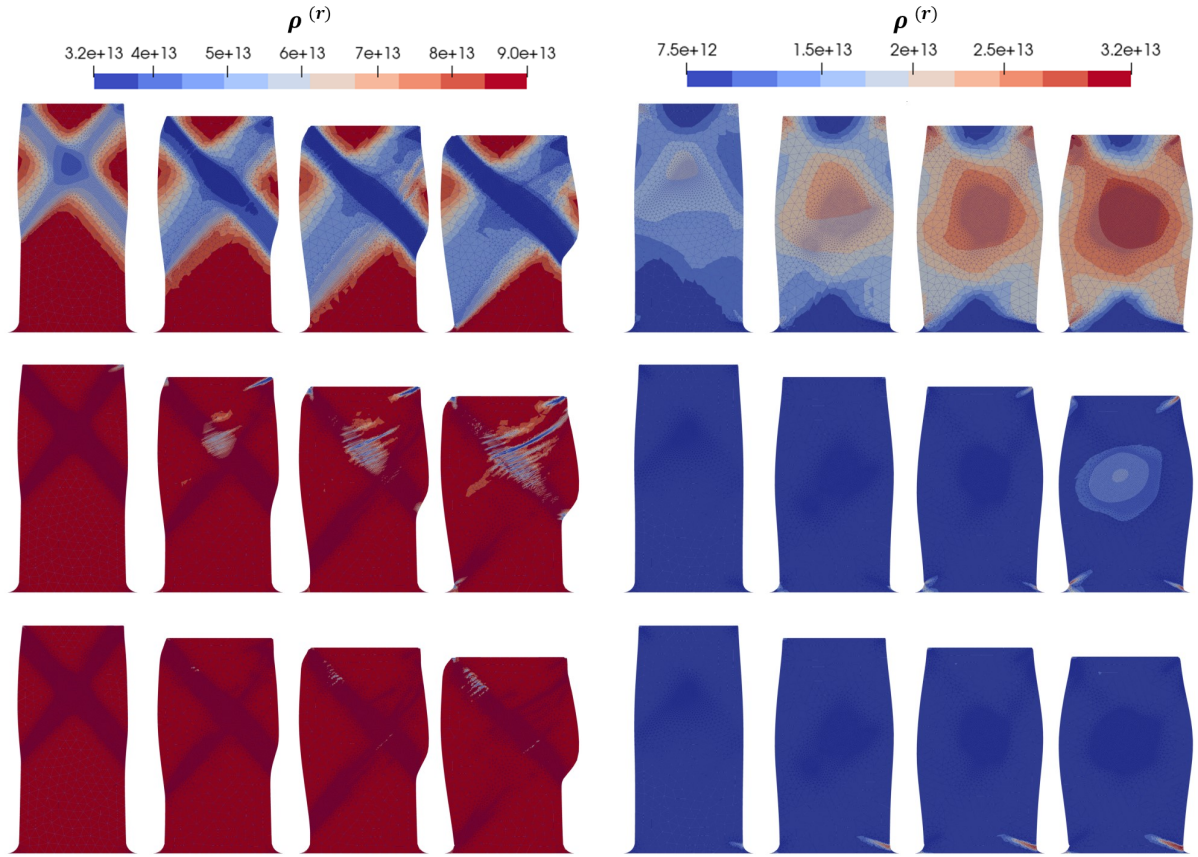


Figure 11: Pillar deformation for the self interaction model. Dislocation densities ρ^1 (up), ρ^2 (middle) and ρ^3 (bottom) distributions (in m^{-2}) at different levels of engineering deformations (5%, 10%, 14% and 18%) for two choices of initial dislocation densities: case (i) (left) and case (ii) (right).

Saturation of dislocation densities. The saturation of the computed dislocation densities starts at a high level of deformation and affects only system 1. This is evident for case (i) at 12.5% of engineering deformation and for case (ii) at 18%. The delayed saturation of dislocation densities in case (ii) is attributed to the substantial difference in slip values, γ^1 , between the two cases at an equivalent total deformation. At 12.5% of engineering strain, the mean slip value γ^1 was around 90% in the shear band for case (i), while for case (ii), it did not even reach 40%. These results confirm that saturation occurs for larger values of slip (more than 50%), as pointed out by the previous stability analysis.

Shear bands. Altogether, this means that when dealing with softening processes (as in the case (i)), plastic deformation tends to favor the propagation along a specific slip system, leading to one or two shear bands. When hardening is present (as in the case (ii)), shear bands cannot develop significantly, as the plastic yield limit increases with the slip accumulated in the shear band. This is why we observe a multitude of small shear bands, and an "isotropization" is induced by the presence of multi-slips in different regions of the pillar, resulting in an overall homogeneous deformation.

Role played by the initial lattice orientation θ^0 . The simulation results presented earlier are based on an initial crystal lattice orientation of $\theta^0 = 65^\circ$, which serves as the reference configuration. Our goal is to investigate how the activity of slip systems evolves with different initial orientations. To explore the impact of the initial lattice orientation on localized plastic deformation (case (i)), we conducted additional simulations under the same conditions but with three distinct initial orientations: $\theta^0 = 35^\circ$, $\theta^0 = 145^\circ$, and $\theta^0 = 115^\circ$, depicted in Fig. 12. For $\theta^0 = 35^\circ$, as shown in Fig. 12(a), the simulation reveals a multislip scenario, characterized by two localized shear bands instead of just one. Interestingly, these shear bands exhibit divergent orientations, appearing to point in opposite directions. Unlike the reference configuration, system 1 is no longer active, allowing systems 2 and 3 to accommodate the deformation. Assuming that we initially rotate the crystal by $\frac{\pi}{2}$ from the reference configuration, no change in the deformation pattern is observed; deformation localizes exactly as it does in the reference configuration. This consistency persists even when the reference configuration is set at an angle of 35° . Alternatively, when the initial rotation angle is set as $\pi - \theta$, an intriguing shift in behavior is observed. The shearing direction is inverted relative to the shearing direction associated with the θ orientation, exhibiting mirror symmetry, as shown in Fig. 12. Irrespective of the specific initial angle θ^0 chosen, a consistent observation emerges: stable stationary shear bands form with an absolute angle between 45° and 55° .

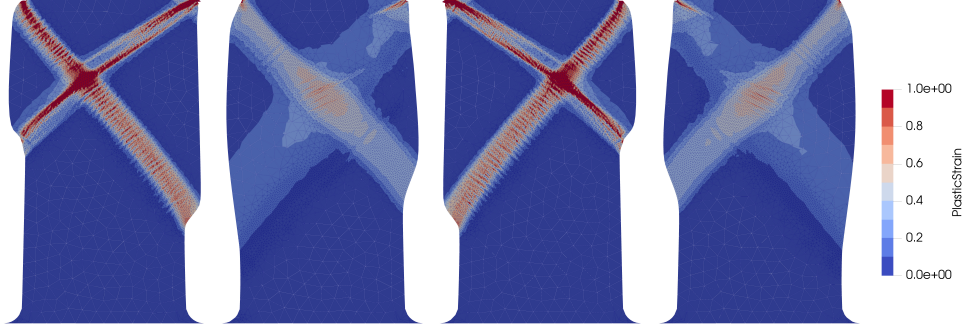


Figure 12: Pillar final deformation for the self interaction model in case (i). The distribution of cumulated plastic strain at $\varepsilon^{engn} = 11\%$ for different initial orientations of the crystal $\theta^0 = 35^\circ; 65^\circ; 145^\circ$ and 115° .

4.6 Cross-interaction simulations

In this section, we explore the features captured by cross-interaction calculations and compare them to the results from self-interaction. .

Final shape. Notably, for case (ii), the deformation process (i.e., the final shape) remains qualitatively unchanged, consistently exhibiting a hardening process characterized by diffusive overall deformation. However, a distinctive observation emerges in the case (i). Here, the cross-interaction case reveals aspects related to dislocation interactions between different systems that are not captured by the self-interaction model. The difference between this case and self-computation becomes evident in this context.

Slip rates. Examining Fig. 13, which depicts the spatial slip rate distributions, we observe similarities between the cross and self-interaction computations. In both samples, slip system 3 remains inactive during deformation, while slip system 1 is consistently active. Significantly, the activation of system 2—occurring at a later deformation stage (beyond 14%)—partly obstructs the activity of system 1, constituting a clear divergence between the cross and self-interaction computations. In the cross-interaction computation, the slip motion orientation is no longer dictated solely by system 1, in contrast to the self-interaction model. Instead, the slip direction is influenced by both systems 1 and 2, with a bias toward system 1.

Evolution of dislocation densities. According to the above observation concerning the active slip systems we conclude that this situation corresponds to case (a) of the stability analysis of section 4.2.2 and depicted in Figure 6. The evolution of spatial distributions of dislocation densities in the cross interaction computation are shown in Fig. 14.

Saturation of dislocation densities. In case (ii), the stability analysis predicts an increase in the dislocation density of system 1, which is associated with a hardening process, unlike the plateau observed in case (i). This leads to a change in the deformation

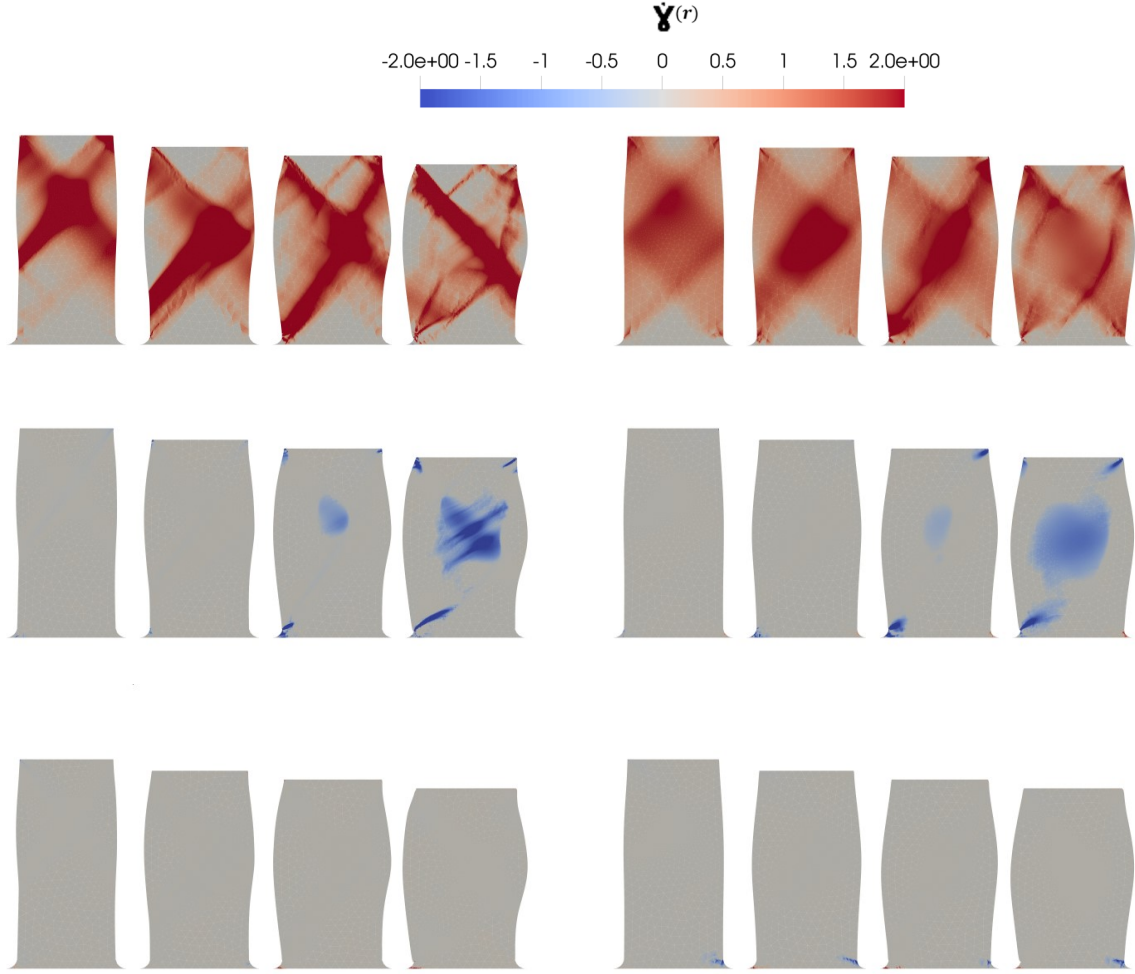


Figure 13: Simulation with the cross-interaction (KM) model. The slip rates $\dot{\gamma}_1$ (up), $\dot{\gamma}_2$ (middle) and $\dot{\gamma}_3$ (bottom) distribution (in sec^{-1}) at different levels of engineering deformations (5%, 10%, 14% and 18%). Left: case (i) (associated to $D = 1\mu\text{m}$). Right: case (ii) (associated to $D = 20\mu\text{m}$).

mode of the pillar: shear bands cannot form, and instead, diffuse deformation is observed. This implies that the slip strain is insufficient for system 1 (and eventually system 2) to reach the saturation dislocation density and the corresponding saturation yield stress $\tau_{c,\text{sat}}^{1,(ii)}$.

5 Conclusions

Dislocation-density based crystal plasticity models are introduced to account for the microstructural changes throughout the deformation process, enabling more accurate predictions of deformation process compared to slip-system resistance-based plasticity models.

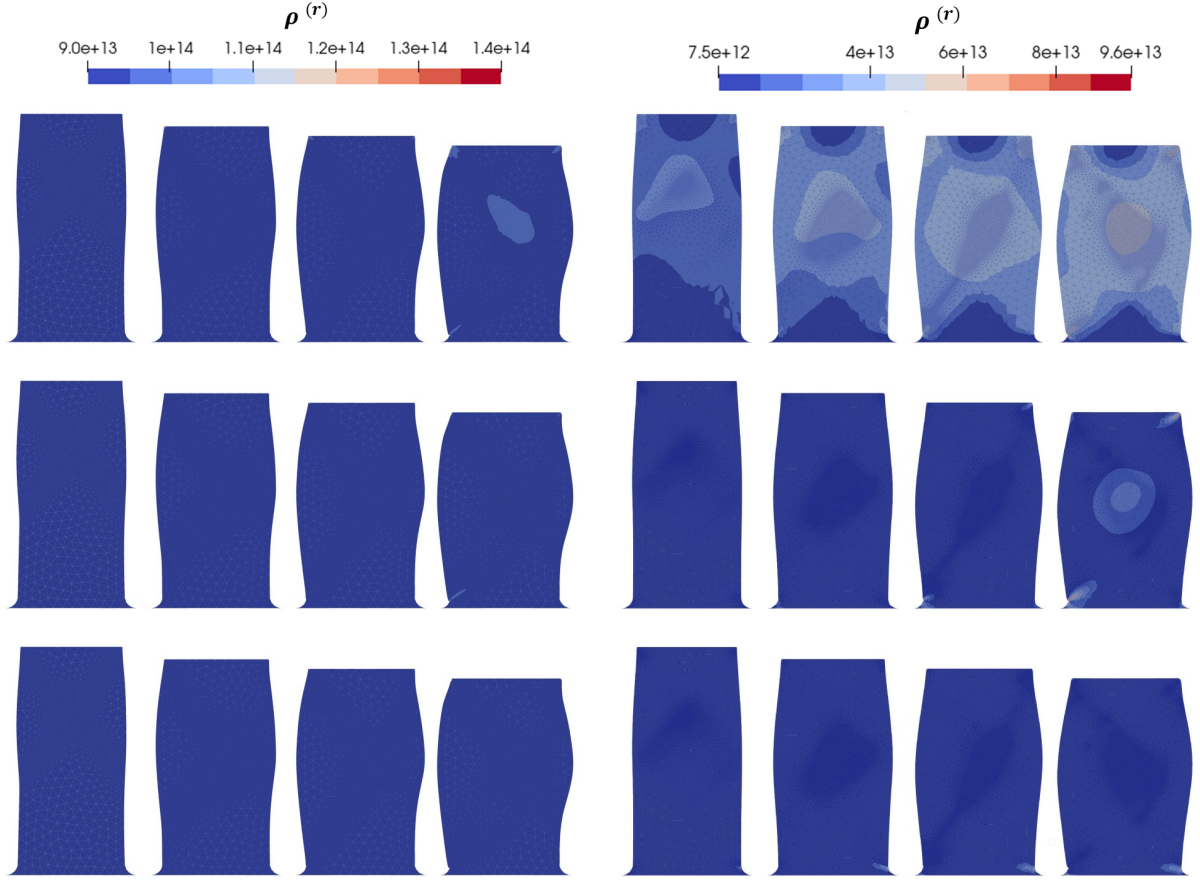


Figure 14: Simulation with the cross-interaction (KM) model. Dislocation densities ρ^1 (up), ρ^2 (middle) and ρ^3 (bottom) distributions (in m^{-2}) at different levels of engineering deformations (5%, 10%, 14% and 18%). Left: case (i) (associated to $D = 1\mu\text{m}$). Right: case (ii) (associated to $D = 20\mu\text{m}$).

In this work, we presented a stability analysis of some established dislocation density-based models, including the Kocks and Mecking (KM) model and its variants, aiming to identify conditions for stationary states in active slip systems and evaluate their linear stability. Our analysis can be generalized to any type of dislocation density model, providing a broader framework for understanding the stability of such systems. Following this analysis, we find the presence of saturated dislocation densities and the essential role of initial dislocation density in distinguishing between hardening and softening responses. Given that the initial dislocation density could be related to the sample's size or preparation process, size-effects can potentially be captured.

Finally, we conducted numerical simulations of micro-pillar compression using an Eulerian crystal plasticity approach to address the behavior of materials at micro-scale dimensions. Our findings indicate that microstructural evolution in small-scale materials can be effectively modeled using dislocation-density based CP models, providing valuable insights for the design of miniaturized mechanical devices and advanced materials in the rapidly evolving field of nanotechnology. To be more precise, the impact of initial dislocation density on the mechanical response in monocrystals is significant, as shown in several studies [71, 72, 73, 74]. These studies emphasize that variations in microstructure, particularly initial dislocation density, can arise due to differences in sample size and/or fabrication methods.

For instance, the situation when the fabrication method change or alters the microstructure, micro-pillars milled from bulk single crystals using a focused ion beam (FIB), this process shapes the pillars by bombarding the target's surface with gallium-accelerated heavy ions, modifying the microstructure of specimens with a large surface-to-volume ratio. This modification includes introducing an additional dislocation network, decorating dislocations with gallium, or forming gallium precipitates [75]. The FIB preparation effect on mechanical response is strong for ordered bulk material (low dislocation density) and becomes more pronounced with decreasing sample size. As a result, the initial dislocation density increases with decreasing sample dimensions [38]. This inverse relationship between sample size and initial dislocation density is referred to in the literature as a "size-effect", which is notably absent in conventional bulk plasticity. Furthermore, it has been reported that regardless of sample preparation, two (Cu) nano specimens with the same initial microstructure exhibit identical mechanical responses, even if their sizes differ [34]. This observation suggests that the initial microstructure may have a more significant impact than size, leading to a preference for discussing the "initial microstructure effect" rather than the "size-effect".

References

- [1] B. Devincre, T. Hoc, and L. Kubin. Dislocation mean free paths and strain hardening of crystals. *Science*, 320(5884):1745–1748, 2008.
- [2] Yinan Cui, Giacomo Po, Pratyush Srivastava, Katherine Jiang, Vijay Gupta, and Nasr Ghoniem. The role of slow screw dislocations in controlling fast strain avalanche dynamics in body-centered cubic metals. *Int. J. Plast.*, 124:117–132, January 2020.
- [3] S. A. Habib, J. T. Lloyd, C. S. Meredith, A. S. Khan, and S. E. Schoenfeld. Fracture of an anisotropic rare-earth-containing magnesium alloy (zek100) at different stress states and strain rates: Experiments and modeling. *Int. J. Plast.*, 122:285–298, 2019.
- [4] A. Irastorza-Landa, H. Van Swygenhoven, S. Van Petegem, N. Grilli, A. Bollhalder, S. Brandstetter, and D. Grolimund. Following dislocation patterning during fatigue. *Acta Mater.*, 112:184–193, 2016.
- [5] He-Jie Guo, Chao Ling, Esteban P Busso, Zheng Zhong, and Dong-Feng Li. Crystal plasticity based investigation of micro-void evolution under multi-axial loading conditions. *Int. J. Plast.*, 129(102673), 2020.
- [6] Nikoletta G Prastiti, Yilun Xu, Daniel S Balint, and Fionn P E Dunne. Discrete dislocation, crystal plasticity and experimental studies of fatigue crack nucleation in single-crystal nickel. *Int. J. Plast.*, 126(102615):102615, March 2020.
- [7] N. Takata, S. Uesugi, T. Zhu, S. Takeyasu, A. Suzuki, and M. Kobashi. Influence of dislocation substructure on size-dependent strength of high-purity aluminum single-crystal micropillars. *Mater. Trans.*, 64(8):1952–1958, 2023.
- [8] P. Zhang, O. U. Salman, J. Zhang, G. Liu, J. Weiss, L. Truskinovsky, and J. Sun. Taming intermittent plasticity at small scales. *Acta Mater.*, 2016.
- [9] Y. Pan, H. Wu, X. Wang, Q. Sun, L. Xiao, X. Ding, J. Sun, and E. K. H. Salje. Rotatable precipitates change the scale-free to scale dependent statistics in compressed ti nano-pillars. *Sci. Rep.*, 9(1):3778, 2019.
- [10] J. Weiss, P. Zhang, O. U. Salman, G. Liu, and L. Truskinovsky. Fluctuations in crystalline plasticity. *C. R. Phys.*, 22(S3):1–37, 2021.
- [11] Bozhao Wu, Yupeng Wu, Yangyang Pan, and Ze Liu. Nanoscale deformation of crystalline metals: Experiments and simulations. *Int. J. Plast.*, 161(103501):103501, February 2023.
- [12] J Wijnjen, T Vermeij, J P M Hoefnagels, M G D Geers, and R H J Peerlings. High-resolution numerical–experimental comparison of heterogeneous slip activity in quasi-2D ferrite sheets. *Int. J. Solids Struct.*, 320(113523):113523, 2025.
- [13] C. Baruffi, A. Finel, Y. Le Bouar, B. Bacroix, and O. U. Salman. Overdamped

- langevin dynamics simulations of grain boundary motion. *Mater. Theory*, 3:1–26, 2019.
- [14] R. Hill. Generalized constitutive relations for incremental deformation of metal crystals by multislip. *J. Mech. Phys. Solids*, 14(2):95–102, 1966.
 - [15] R. Hill and J. R. Rice. analysis of elastic-plastic crystals at arbitrary strain, constitutive. *J. Mech. Phys. Solids*, 20(6):401–413, 1972.
 - [16] R. J. Asaro and J. R. Rice. Strain localization in ductile single crystals. *J. Mech. Phys. Solids*, 25(5):309–338, 1977.
 - [17] R. J. Asaro. Crystal plasticity. *J. Appl. Mech.*, 50(4b):921–934, 1983.
 - [18] D. Peirce, R. J. Asaro, and A. Needleman. Material rate dependence and localized deformation in crystalline solids. *Acta Metall.*, 31(12):1951–1976, 1983.
 - [19] F. Roters, P. Eisenlohr, L. Hantcherli, D. D. Tjahjanto, T. R. Bieler, and D. Raabe. Overview of constitutive laws, kinematics, homogenization and multiscale methods in crystal plasticity finite-element modeling: Theory, experiments, applications. *Acta Mater.*, 58(4):1152–1211, 2010.
 - [20] M Lamari, P Kerfriden, O U Salman, V Yastrebov, K Ammar, and S Forest. A time-discontinuous elasto-plasticity formalism to simulate instantaneous plastic flow bursts. *Int. J. Solids Struct.*, 309(113171):113171, March 2025.
 - [21] Amirhossein Lame Jouybari, Samir El Shawish, and Leon Cizelj. Fast fourier transform approach to strain gradient crystal plasticity: Regularization of strain localization and size effect. *Int. J. Plast.*, 183(104153):104153, December 2024.
 - [22] C. Hardie, D. J. Long, E. Demir, E. Tarleton, and F. P.E. Dunne. A robust and efficient hybrid solver for crystal plasticity. *International Journal of Plasticity*, 170:103773, 2023.
 - [23] L. Cai, M. Jebahi, and F. Abed-Meraim. Strain localization modes within single crystals using finite deformation strain gradient crystal plasticity. *Crystals*, 11(10):1235, 2021.
 - [24] Zhang X., Zhao J., Kang G., and Zaiser M. Geometrically necessary dislocations and related kinematic hardening in gradient grained materials: A nonlocal crystal plasticity study. *Int. J. Plast.*, 163:103553, 2023.
 - [25] Cappola J., n Wang J., and Li L. A dislocation-density-based crystal plasticity model for fcc nanocrystalline metals incorporating thermally-activated depinning from grain boundaries. *Int. J. Plast.*, 172:103863, 2024.
 - [26] Fischer T., Xiang S., Dahlberg C. F.O., and Hedström P. Creep-fatigue properties of austenitic cast iron d5s with tension and compression dwell: A dislocation density-

- based crystal plasticity study. *Mater. Sci. Eng. A*, 860:144212, 2022.
- [27] Hunter A. and Preston D. L. Analytic model of dislocation density evolution in fcc polycrystals accounting for dislocation generation, storage, and dynamic recovery mechanisms. *Int. J. Plast.*, 151:103178, 2022.
 - [28] Eghtesad A., Luo Q., Shang S.-L., Lebensohn R. A., Knezevic M., Liu Z.-K., and Allison M. Beese. Machine learning-enabled identification of micromechanical stress and strain hotspots predicted via dislocation density-based crystal plasticity simulations. *Int. J. Plast.*, 166:103646, 2023.
 - [29] M. Hamid, H. Lyu, B. J. Schuessler, P. C. Wo, and H. M. Zbib. Modeling and characterization of grain boundaries and slip transmission in dislocation density-based crystal plasticity. *Crystals*, 7(6):152, 2017.
 - [30] S. Ghorbanpour, M. Zecevic, A. Kumar, M. Jahedi, J. Bicknell, L. Jorgensen, I. J. Beyerlein, and M. Knezevic. A crystal plasticity model incorporating the effects of precipitates in superalloys: application to tensile, compressive and cyclic deformation of inconel 718. *Int. J. Plast.*, 99:162–185, 2017.
 - [31] C. Ye, G. Liu, K. Chen, J. Liu, J. Hu, Y. Yu, Y. Mao, and Y. Shen. Unified crystal plasticity model for fcc metals: From quasistatic to shock loading. *Phys. Rev. B Condens. Matter*, 107(2):024105, 2023.
 - [32] A. J. Cackett, C. D. Hardie, J. J. Lim, and E. Tarleton. Spherical indentation of copper: Crystal plasticity vs experiment. *Materialia*, 7:100368, 2019.
 - [33] S. Agaram, A. K. Kanjarla, B. Bhuvanaraghan, and S. M. Srinivasan. Dislocation density based crystal plasticity model incorporating the effect of precipitates in IN718 under monotonic and cyclic deformation. *Int. J. Plast.*, 141:102990, 2021.
 - [34] A. T. Jennings, M. J. Burek, and J. R. Greer. Microstructure versus size: Mechanical properties of electroplated single crystalline cu nanopillars. *Phys. Rev. Lett.*, 104(13):135503, 2010.
 - [35] H. Guo, C. Li, X. Zhang, and F. Shang. The strain hardening of micro-sized face-centered-cubic single crystal metals: A crystal plasticity study. *AIP Advances*, 8(12):125208, 2018.
 - [36] Triplicane A. Parthasarathy, Satish I. Rao, D. M. Dimiduk, M. D. Uchic, and D. R. Trinkle. Contribution to size effect of yield strength from the stochastics of dislocation source lengths in finite samples. *Scr. Mater.*, 56(4):313–316, 2007.
 - [37] D. Kurunczi-Papp and L. Laurson. Avalanches and rate effects in strain-controlled discrete dislocation plasticity of al single crystals. *Phys. Rev. Mater.*, 7(1):013605, 2023.

- [38] Y.N. Cui, P. Lin, Z.L. Liu, and Z. Zhuang. Theoretical and numerical investigations of single arm dislocation source controlled plastic flow in fcc micropillars. *Int. J. Plast.*, 55:279–292, 2014.
- [39] W. Zeng, J. M. Larsen, and G. R. Liu. Smoothing technique based crystal plasticity finite element modeling of crystalline materials. *Int. J. Plast.*, 65:250–268, 2015.
- [40] K. Nguyen, M. Zhang, V. J. Amores, M. A. Sanz, and F. J. Montáns. Computational modeling of dislocation slip mechanisms in crystal plasticity: a short review. *Crystals*, 11(1):42, 2021.
- [41] R. Baggio, P. Biscari, S. Conti, L. Truskinovsky, G. Zanzotto, and O. Salman. Landau-type theory of planar crystal plasticity. *Phys. Rev. Lett.*, 123(20):205501, 2019.
- [42] J. R. Rice. constitutive relations for solids: An internal-variable theory, inelastic and its application to metal plasticity. *J. Mech. Phys. Solids*, 19(6):433–455, 1971.
- [43] C. Teodosiu and F. Sidoroff. A theory of finite elastoviscoplasticity of single crystals. *Int. J. Eng. Sci.*, 14(2):165–176, 1976.
- [44] R.J. Asaro and A. Needleman. Overview no. 42 texture development and strain hardening in rate dependent polycrystals. *Acta Metall.*, 33(6):923–953, 1985.
- [45] G. I. Taylor. The mechanism of plastic deformation of crystals. part i.—theoretical. *Proceedings of the Royal Society of London. Series A, Containing Papers of a Mathematical and Physical Character*, 145(855):362–387, 1934.
- [46] C. Teodosiu, J. Raphanel, and L. Tabourot. Finite element simulation of the large elastoplastic deformation of multicrystals. In *Proceedings of the International Seminar MECAMAT’91*, pages 153–168, Fontainebleau, France, August 1991. ISBN 9054103175.
- [47] P. Franciosi, M. Berveiller, and A. Zaoui. Latent hardening in copper and aluminium single crystals. *Acta Metall.*, 28(3):273–283, 1980.
- [48] H. Mecking and K. Lucke. A new aspect of the theory of flow stress of metals. *Scr. Metall.*, 4(6):427–432, 1970.
- [49] L. Kubin, B. Devincre, and T. Hoc. Modeling dislocation storage rates and mean free paths in face-centered cubic crystals. *Acta Mater.*, 56(20):6040–6049, 2008.
- [50] I.S. Yasnikov, Y. Kaneko, M. Uchida, and A. Vinogradov. The grain size effect on strain hardening and necking instability revisited from the dislocation density evolution approach. *Mater. Sci. Eng. A*, 831:142330, 2022.
- [51] T. Kameda and M.A. Zikry. Three dimensional dislocation-based crystalline constitutive formulation for ordered intermetallics. *Scr. Mater.*, 38(4):631–636, 1998.

- [52] J. Alcala, O. Casals, and J. Ocenasek. Micromechanics of pyramidal indentation in fcc metals: Single crystal plasticity finite element analysis. *J. Mech. Phys. Solids*, 56(11):3277–3303, 2008.
- [53] Y. Estrin and H. Mecking. A unified phenomenological description of work hardening and creep based on one-parameter models. *Acta Metall.*, 32(1):57–70, 1984.
- [54] J. Dequiedt, C. Denoual, and R. Madec. Heterogeneous deformation in ductile fcc single crystals in biaxial stretching: the influence of slip system interactions. *J. Mech. Phys. Solids*, 83:301–318, 2015.
- [55] R. Madec and L. P. Kubin. Dislocation strengthening in fcc metals and in bcc metals at high temperatures. *Acta Mater.*, 126:166–173, 2017.
- [56] O. Cazacu and I. R. Ionescu. Dynamic crystal plasticity: An Eulerian approach. *J. Mech. Phys. Solids*, 58(6):844–859, 2010.
- [57] O. Friderikos, D. Sagris, C. N. David, and A. Korlos. Simulation of adiabatic shear bands in orthogonal machining of Ti6Al4V using a rigid-viscoplastic finite element analysis. *Metals*, 10(3):338, 2020.
- [58] R.A. Lebensohn and C.N. Tomé. A self-consistent anisotropic approach for the simulation of plastic deformation and texture development of polycrystals: Application to zirconium alloys. *Acta Metall. Mater.*, 41(9):2611–2624, 1993.
- [59] S. Kok, A.J. Beaudoin, and D.A. Tortorelli. A polycrystal plasticity model based on the mechanical threshold. *Int. J. Plast.*, 18(5):715–741, 2002.
- [60] J. Smiri. *Large plastic deformation of crystals: stability analysis and attractors*. PhD thesis, Université Paris-Nord-Paris XIII, 2024.
- [61] O. U. Salman and I. R. Ionescu. Tempering the mechanical response of FCC micropillars: An Eulerian plasticity approach. *Mech. Res. Commun.*, 114(103665):103665, 2021.
- [62] J. Crepin, T. Bretheau, and D. Caldemaison. growth, cavity and rupture of β -treated zirconium: A crystallographic model. *Acta Mater.*, 44(12):4927–4935, 1996.
- [63] Oana Cazacu and Ioan R. Ionescu. Augmented Lagrangian method for Eulerian modeling of viscoplastic crystals. *Comput. Methods Appl. Mech. Eng.*, 199(9):689–699, 2010.
- [64] J. Smiri, O. U. Salman, and I. R. Ionescu. Accounting for localized deformation: a simple computation of true stress in micropillar compression experiments. *Exp. Mech.*, 64(9):1435–1442, 2024.
- [65] J. C. Simo and T. J. Hughes. *Computational inelasticity*, volume 7. Springer Science & Business Media, 2006.

- [66] R. Glowinski and P. Le Tallec. *Augmented Lagrangian and Operator Splitting Methods in Nonlinear Mechanics*. SIAM Studies in Applied Mathematics. Society for Industrial and Applied Mathematics (SIAM), Philadelphia, PA, 1989.
- [67] I. R. Ionescu. Onset and dynamic shallow flow of a viscoplastic fluid on a plane slope. *J. Non-Newtonian Fluid Mech.*, 165(19-20):1328–1341, 2010.
- [68] I. R. Ionescu. Augmented lagrangian for shallow viscoplastic flow with topography. *J. Comput. Phys.*, 242:544–560, 2013.
- [69] R. Jafari and T. Okutucu-Özyurt. 3d numerical modeling of boiling in a microchannel by arbitrary Lagrangian-Eulerian (ALE) method. *Appl. Math. Comput.*, 272:593–603, 2016.
- [70] F. Duarte, R. Gormaz, and S. Natesan. Arbitrary Lagrangian–Eulerian method for Navier–Stokes equations with moving boundaries. *Comput. Methods Appl. Mech. Eng.*, 193(45–47):4819–4836, 2004.
- [71] D.M. Norfleet, D.M. Dimiduk, S.J. Polasik, M.D. Uchic, and M.J. Mills. Dislocation structures and their relationship to strength in deformed nickel microcrystals. *Acta Mater.*, 56(13):2988–3001, 2008.
- [72] Cynthia M. Byer and K.T. Ramesh. Effects of the initial dislocation density on size effects in single-crystal magnesium. *Acta Mater.*, 61(10):3808–3818, 2013.
- [73] H. Bei, S. Shim, E.P. George, M.K. Miller, E.G. Herbert, and G.M. Pharr. Compressive strengths of molybdenum alloy micro-pillars prepared using a new technique. *Scr. Mater.*, 57(5):397–400, 2007.
- [74] A. Rinaldi, P. Peralta, K. Sieradzki, E. Traversa, and S. Licoccia. Role of dislocation density on the sample-size effect in nanoscale plastic yielding. *J. Nanomech. Micromech.*, 2(3):42–48, 2012.
- [75] L. Borasi, A. Slagter, A. Mortensen, and C. Kirchlechner. On the preparation and mechanical testing of nano to micron-scale specimens. *Acta Mater.*, 283:120394, 2024.